ADJOINT BASED AERODYNAMIC SHAPE OPTIMIZATION OF A MISSILE ENGINE INLET COVER

A THESIS SUBMITTED TO
THE GRADUATE SCHOOL OF NATURAL AND APPLIED SCIENCES
OF
MIDDLE EAST TECHNICAL UNIVERSITY

BY

ARDA ÖZUZUN

IN PARTIAL FULFILLMENT OF THE REQUIREMENTS
FOR
THE DEGREE OF MASTER OF SCIENCE
IN
AEROSPACE ENGINEERING

JUNE 2024

Approval of the thesis:

ADJOINT BASED AERODYNAMIC SHAPE OPTIMIZATION OF A MISSILE ENGINE INLET COVER

submitted by **ARDA ÖZUZUN** in partial fulfillment of the requirements for the degree of **Master of Science in Aerospace Engineering Department, Middle East Technical University** by,

Prof. Dr. Naci Emre Altun
Dean, Graduate School of **Natural and Applied Sciences** _____

Prof. Dr. Serkan Özgen
Head of Department, **Aerospace Engineering** _____

Prof. Dr. İsmail Hakkı Tuncer
Supervisor, **Aerospace Engineering, METU** _____

Examining Committee Members:

Prof. Dr. Yusuf Özyörük
Aerospace Engineering, METU _____

Prof. Dr. İsmail H. Tuncer
Aerospace Engineering, METU _____

Prof. Dr. Sinan Eyi
Aerospace Engineering, METU _____

Prof. Dr. Hasan U. Akay
Mechanical Engineering, Atılım University _____

Assoc. Prof. Dr. Mustafa Kaya
Aerospace Engineering, Ankara Yıldırım Beyazıt University _____

Date:27.06.2024

I hereby declare that all information in this document has been obtained and presented in accordance with academic rules and ethical conduct. I also declare that, as required by these rules and conduct, I have fully cited and referenced all material and results that are not original to this work.

Name, Surname: Arda Özuzun

Signature :

ABSTRACT

ADJOINT BASED AERODYNAMIC SHAPE OPTIMIZATION OF A MISSILE ENGINE INLET COVER

Özuzun, Arda
M.S., Department of Aerospace Engineering
Supervisor: Prof. Dr. İsmail Hakkı Tuncer

June 2024, 72 pages

This thesis addresses the aerodynamic shape optimization of a missile engine inlet cover, a component designed to prevent windmilling on the gas turbine engines during the gliding phase of the missiles. The adjoint-based optimization is conducted with the open-source SU2 software suite. The cover shape is controlled by means of a Free Form Deformation box control points. The design objectives are to minimize the drag and maximize the opening moment of the inlet cover at the same time. Both single and multi-objective optimizations with weight factors are performed. The findings are discussed in detail, and it is shown that the optimization process provides new cover shapes for increased aerodynamic performance compared to the quarter-spherical baseline cover.

Keywords: Computational Fluid Dynamics, Aerodynamic Shape Design, Adjoint-based optimization, Free Form Deformation Box, SU2

ÖZ

ADJOINT YÖNTEMİ İLE FÜZE HAVA ALIĞI KAPAĞININ AERODİNAMİK ŞEKİL OPTİMİZASYONU

Özuzun, Arda
Yüksek Lisans, Havacılık ve Uzay Mühendisliği Bölümü
Tez Yöneticisi: Prof. Dr. İsmail Hakkı Tuncer

Haziran 2024 , 72 sayfa

Bu tez, füze motoru hava alığı kapağının aerodinamik şekil optimizasyonunu ele almaktadır. Hava alığı kapağı, füzenin süzülme esnasında gaz türbin motor pallerinin akış etkisiyle dönmesini önlemek için kullanılan bir bileşendir. Gradyan tabanlı aerodinamik şekil optimizasyonu, açık kaynak kodlu SU2 yazılımı kullanılarak ayrık adjoint yöntemi ile gerçekleştirilmiştir. Kapak yüzeyi, Serbest Form Deformasyon kutusu kontrol noktaları aracılığıyla deforme edilmiştir. Tasarım hedefi, süzülme sırasında sürüklenme kuvvetini en aza indirgemek ve hava alığı kapağının menteşe eksenine göre açılma momentini artırmaktır. Tek ve çoklu amaçlı optimizasyon çalışmaları yürütülmüştür. Bulgular detaylı bir şekilde incelenmiş ve optimizasyon sürecinde, çeyrek küre şeklindeki temel tasarıma göre daha üstün aerodinamik performans sağlayan yeni kapak şekilleri elde edilmiştir.

Anahtar Kelimeler: Hesaplamalı Akışkanlar Dinamiği, Aerodinamik Yüzey Optimizasyonu, Adjoint Tabanlı Optimizasyon, Serbest Form Deformasyon, SU2

To my family

ACKNOWLEDGMENTS

I extend my deepest gratitude to Prof. Dr. İsmail Hakkı Tuncer for his continuous support, constructive criticism, and valuable guidance throughout my M.Sc. journey. His expertise and profound insights have not only shaped my thesis but have also significantly contributed to my academic growth.

I would also like to thank my colleagues and managers in the Aerodynamic Design and Analysis Department of Roketsan for their support. I want to express my sincere gratitude to Ulaş Canberk Ayan, Tezcan Ünlü, and Ertan Demiral for their comments and assistance in overcoming challenges during the thesis.

Special thanks to my dear friends Mustafa Orhan, Kuzey Koçal, Tutku Ilgın Özcan, Utku Yücel, and Mahmut Arıcan for their valuable friendship.

I am always grateful to my parents, Maide Özuzun and Mehmet Özuzun, and my brother, Mustafa Özuzun, for their unwavering support, motivation, and boundless love.

TABLE OF CONTENTS

ABSTRACT v

ÖZ vi

ACKNOWLEDGMENTS viii

TABLE OF CONTENTS ix

LIST OF TABLES xi

LIST OF FIGURES xii

LIST OF ABBREVIATIONS xvi

CHAPTERS

1 INTRODUCTION 1

1.1 Inlet Cover 3

1.2 Adjoint-based Optimization Studies 5

1.3 Objectives and Outline of the Thesis 6

2 METHODOLOGY 9

2.1 Flow Solution with SU2 9

2.1.1 Turbulence Modelling 10

2.1.2 Solver Settings 11

2.2 Gradient Based Optimization 12

2.3 Discrete Adjoint Method 14

2.3.0.1 Evaluation of Surface Sensitivity Derivatives 16

2.4 Free Form Deformation Box 16

2.5 FADO: Framework for Aerostructural Design Optimization 18

3 RESULTS AND DISCUSSION 23

3.1 Baseline Configuration 24

3.2 Design Condition 26

3.3 Verification Studies 27

3.3.1 Hemisphere Cylinder Test Case 28

3.3.2 NASA TM X-3070 Missile Test Case 32

3.4 Grid Independence Study for the Baseline Configuration 38

3.5 Parallel Performance of the SU2 Flow Solver 43

3.6 Aerodynamic Shape Optimization Studies 43

3.6.1 Free Form Deformation Box and Geometric Constraints 45

3.6.2 Case I: Minimization of the Inlet Cover Drag 45

3.6.3 Case II: Constrained Maximization of the Inlet Cover Opening Moment 53

3.6.4 Case III: Multi-objective Optimization 58

4 CONCLUSIONS 65

REFERENCES 67

LIST OF TABLES

TABLES

Table 3.1 Design Condition 27

Table 3.2 Test Condition for the Hemisphere Cylinder 29

Table 3.3 Grid Data for the Hemisphere Cylinder 30

Table 3.4 Test Condition for NASA TM X-3070 Missile 32

Table 3.5 Grid Data for NASA TM X-3070 Missile 34

Table 3.6 Grid Data for Baseline Configuration 39

Table 3.7 Turbulence Model Predictions 42

Table 3.8 Aerodynamic Loads for Case I 51

Table 3.9 Aerodynamic Loads for Case II 56

Table 3.10 Aerodynamic Loads for the Optimum Designs 64

LIST OF FIGURES

FIGURES

Figure 1.1 Tomahawk Missile with Pitot Type Inlet 2

Figure 1.2 SOM-J Cruise Missile 3

Figure 1.3 SOM Cruise Missile 3

Figure 1.4 Illustration of Inlet Cover 4

Figure 2.1 Illustration of Gradient-Based Optimization 12

Figure 2.2 Example Computational Graph 14

Figure 2.3 Drag Sensitivity of OneraM6 Wing 17

Figure 2.4 FFD Box over a Wing-Body Configuration 18

Figure 2.5 Optimization Process 20

Figure 3.1 ÇAKIR Cruise Missile 24

Figure 3.2 Baseline Configuration 25

Figure 3.3 Cross Sectional View of the Inlet Cover 25

Figure 3.4 Components of Baseline Inlet Cover Configuration 26

Figure 3.5 Operational Envelope of a Subsonic Airbreathing Missile 27

Figure 3.6 Wind Tunnel Model for the Hemisphere Cylinder 28

Figure 3.7 Hemisphere Cylinder Model 29

Figure 3.8 Grid Independence Study for Hemisphere Cylinder 30

Figure 3.9 Surface Pressure Distribution along the Hemisphere Cylinder . . 31

Figure 3.10 Variation of y^+ along the Hemisphere Cylinder for Fine Grid . . 31

Figure 3.11 Surface Pressure Distribution along the Hemisphere Cylinder for Fine Grid 31

Figure 3.12 Wind Tunnel Model for NASA TM X-3070 Missile 33

Figure 3.13 Technical Drawing of NASA TM X-3070 Missile 33

Figure 3.14 Solid Model for NASA TM X-3070 Missile 34

Figure 3.15 Grid Independence Study for NASA TM X-3070 Missile 35

Figure 3.16 Variation of Drag Coefficient 37

Figure 3.17 Variation of the Lift Coefficient 37

Figure 3.18 Variation of the Moment Coefficient 37

Figure 3.19 Grid Independence Study for Baseline Configuration 39

Figure 3.20 Drag Coefficient 40

Figure 3.21 Lift Coefficient 40

Figure 3.22 Moment Coefficient 40

Figure 3.23 Front View of the Surface Mesh for the Baseline Configuration . 41

Figure 3.24 Side View of the Surface Mesh for the Baseline Configuration . . 41

Figure 3.25 Cross-Section of the Volume Mesh for the Baseline Configuration 41

Figure 3.26 Variation of y^+ along Baseline Configuration 42

Figure 3.27 Parallel Performance of the SU2 Solver 44

Figure 3.28 History of Residuals 44

Figure 3.29 History of Aerodynamic Coefficients 44

Figure 3.30 FFD Box over Inlet Cover 46

Figure 3.31 Control Points of the FFD Box 46

Figure 3.32 FFD Box Resolutions 46

Figure 3.33 Surface Sensitivity of the Baseline Inlet Cover 47

Figure 3.34 Variation of Drag Coefficient on the Inlet Cover through Optimization Steps 47

Figure 3.35 Inlet Cover Profiles through Optimization Steps 49

Figure 3.36 Inlet Cover Shapes through Optimization Steps 49

Figure 3.37 Baseline and Optimum Inlet Cover Shapes 50

Figure 3.38 Surface Pressure Distribution on Baseline (left) and Optimum (right) Inlet Covers 50

Figure 3.39 Pressure Distribution on Symmetry Plane for Baseline (left) and Optimum (right) Configurations 52

Figure 3.40 Mach Number Distribution on Symmetry Plane for Baseline (left) and Optimum (right) Configurations 52

Figure 3.41 Component Drag Coefficients 53

Figure 3.42 Inlet Cover Hinge Axis 54

Figure 3.43 Variation of CM_{cover} and C_D through Optimization Steps 54

Figure 3.44 Variation of Inlet Cover Profiles through Optimization Steps . . . 55

Figure 3.45 Variation of Inlet Cover Shapes through Optimization Steps . . . 57

Figure 3.46 Baseline and Optimum Inlet Cover Shapes 57

Figure 3.47 Surface Pressure Distribution on Baseline (left) and Optimum (right) Inlet Cover 58

Figure 3.48 Pressure Distribution on Symmetry Plane for Baseline (left) and Optimum (right) 59

Figure 3.49 Mach Number Distribution on Symmetry Plane for Baseline (left) and Optimum (right) 59

Figure 3.50 Pareto Front for Optimum Designs 60

Figure 3.51 Inlet Cover Shapes for Optimum Designs 61

Figure 3.52 Surface Pressure Distribution on Optimum Designs 61

Figure 3.53 Pressure Distribution on Symmetry Plane for Optimum Designs . 62

Figure 3.54 Mach Number Distribution on Symmetry Plane for Optimum Designs 62

LIST OF ABBREVIATIONS

ABBREVIATIONS

2D	2 Dimensional
3D	3 Dimensional
CFD	Computational Fluid Dynamics
RANS	Reynolds-Averaged Navier-Stokes
SU2	Stanford University Unstructured
FFD	Free Form Deformation
AD	Automatic Differentiation
FADO	Framework for Aerostructural Design Optimization
JST	Jameson-Schmidt-Turkel
FGMRES	Flexible Generalized Minimum Residual
SLSQP	Sequential Least Squares Quadratic Programming
BFGS	Broyden–Fletcher–Goldfarb–Shanno
COBYLA	Constrained Optimization by Linear Approximation
SST	Shear Stress Transport
SA	Spalart-Allmaras
Re	Reynolds Number
CD	Drag Coefficient
CL	Lift Coeficient
Cm	Moment Coeficient
CD_{cover}	Drag Coefficient of the Inlet Cover
CL_{cover}	Lift Coefficient of the Inlet Cover
CM_{cover}	Moment Coefficient of the Inlet Cover

CHAPTER 1

INTRODUCTION

In modern military operations, UCAVs (Unmanned Combat Aerial Vehicles) and jet fighters are often equipped with guided missiles. Air-breathing cruise missiles are one of them and hold significant importance in military missions due to their ability to hit targets precisely at long distances. Launching these missiles from aerial platforms offers significant strategic advantages. The platforms allow the missile to be used against targets at longer distances thanks to the extended operational range. They also provide flexibility regarding the launching location and timing.

Missiles commonly utilize a variety of propulsion systems, including rocket, turbojet, and ramjet engines. Mission requirements like range, speed, and altitude determine the selection of the propulsion system. Gas turbine engines have emerged as a commonly preferred choice for anti-ship cruise missiles. These engines are preferred for their cost effectiveness, reliability, and ability to deliver high thrust levels, allowing anti-ship cruise missiles to accomplish their operational goals.

Pitot-type inlets can be used in these missiles to supply air to the gas turbine engines. One of the primary motivations for using a pitot-type inlet is to capture clear air unaffected by the missile. As a result, the entry of the boundary layer into the inlet is prevented. The Tomahawk missile with a pitot-type inlet is an example and can be seen in Figure 1.1.

One of the most critical factors in the design of a cruise missile is maximizing its operational range. Therefore, the aerodynamics of the missile play a vital role in achieving low-drag missile configuration. Any protuberance or component on the missile that generates extra drag may significantly reduce its range. As a result, every

Figure 1.1: Tomahawk Missile with Pitot Type Inlet [1]

component mounted on the missile, whether it remains attached for the entire mission or is used during just a part of the mission, must be aerodynamically optimized to maximize the range.

An inlet cover is a component that remains attached to the missile during a specific phase of the mission. It is designed to prevent the entry of foreign objects and airflow into the engine during the missile's carriage by the aircraft. Additionally, once the aircraft launches the missile, the cover still plays a critical role. After launch, the engine cannot be started instantly because specific flight conditions must be met for the ignition. Therefore, the missile glides until it reaches a certain speed. The inlet cover prevents windmilling on the engine during the gliding phase, and it is jettisoned before the engine ignition [2]. This separation process involves the rotational movement of the cover around a hinge axis, thereby facilitating its disengagement from the missile. Pictures of the inlet cover are given in Figure 1.2 and 1.3

Optimizing the aerodynamic shape of the cover is crucial to minimize the drag of the gliding configuration and increase the gliding range. Also, it is desired that the cover have a moment in the opening direction around the hinge axis for safe separation. In this thesis, aerodynamic shape optimization of the inlet cover is carried out using a generic naval cruise missile configuration. Gradient-based optimization is performed using the discrete adjoint method since it offers benefits for optimization problems that have a high number of design variables [3].

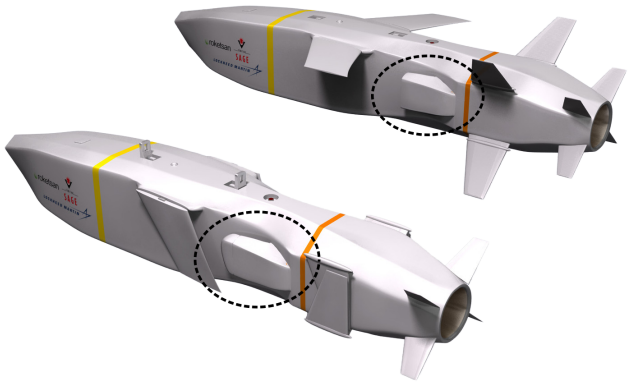

Figure 1.2: SOM-J Cruise Missile

Figure 1.3: SOM Cruise Missile

1.1 Inlet Cover

This section provides a concise overview of the necessity and application of the inlet cover, drawing insights from relevant patents in the field. Aircraft-launched missiles usually experience a period of storage and transportation before they are placed on a launcher that is attached to the aircraft [4]. Subsequently, they remain on the aircraft until there is a potential need for them to be launched. Air-breathing missile systems are equipped with air inlets that supply air to the engine. During this period, it is preferred to coat the inlet of the missile engine to prevent foreign objects from entering the engine. Also, it is vital that in the absence of a cover, the ingress of airflow through the inlet may pose a risk of damaging the rotating components, bearings, and

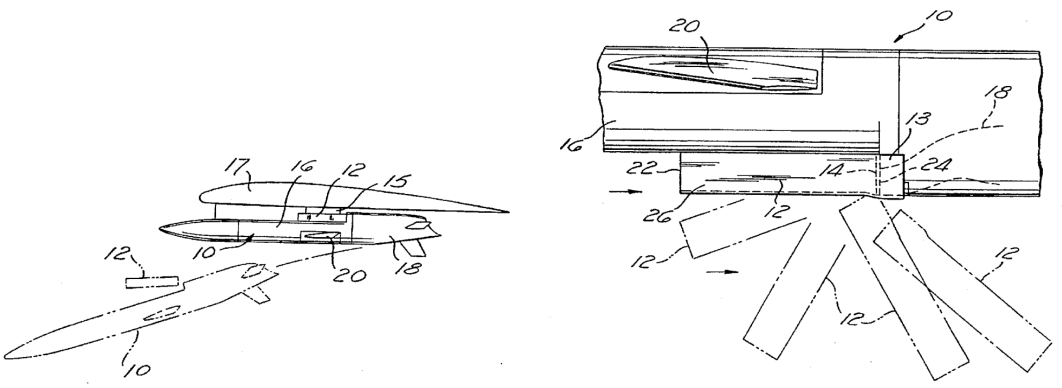

(a) Missile Launch

(b) Inlet Cover Seperation

Figure 1.4: Illustration of Inlet Cover [6]

internal framework of the gas turbine engine before the ignition. The phenomenon is referred to as windmilling, and it has the potential to cause damage to the engine [5]. To eliminate this risk, an inlet cover with a forward shell and a backward attachable end-piece is employed [6]. The cover protects the engine and maintains the missile's operational readiness. The usage of inlet cover is illustrated in Figure 1.4. The cover is represented by the twelfth component in the figure.

After the missile is fired, the engine needs the airflow through the inlet for the ignition. Therefore, the cover on the inlet must be taken off. To remove the inlet cover, various systems employing electrical, mechanical, hydraulic, or pneumatic mechanisms can be utilized [6]. It is critical to consider not only the efficiency of the removal mechanisms but also the effect of these systems on the aerodynamics, weight, and spacing of the missile configuration. Figure 1.4 depicts an illustration of the missile launch from an aircraft and the subsequent removal of the cover. The separation process begins following the trigger activation. The illustration demonstrates the separation process through rotational motion. The motion consists of two phases. In the first phase, the cover rotates about a hinge axis until it reaches a specific point. In the second phase, once the cover reaches this predetermined point, it becomes fully released. At this stage, the cover is free to move with six degrees of freedom. Therefore, the opening aerodynamic moment with respect to the hinge axis is desired to facilitate rotating motion, which streamlines the separation process. Also, the exact point at which the cover achieves full liberation is crucial for its trajectory. A safe trajectory ensures the cover separates smoothly without colliding with the missile.

1.2 Adjoint-based Optimization Studies

The aerodynamic shape optimization methods can be classified into two categories. These are gradient-based and gradient-free methods [7]. The gradient-free or stochastic methods work without the need for gradient calculations. Instead, they explore the design space through randomization or trial-and-error processes in optimization [8]. One prominent example of a gradient-free optimization method is the genetic algorithm. Its role in aerodynamic design is explained in [9]. For instance, aerodynamic shape optimization applications by using genetic algorithms are carried out in [10], [11] and [12].

Although gradient-free methods have benefits in scenarios with multiple local extremes, gradient-based methods offer significant advantages in terms of computational efficiency by reducing the number of function evaluations required, which leads to fewer overall evaluations than gradient-free methods. Therefore, researchers and engineers frequently utilize gradient-based methods in aerodynamic shape optimization problems [13]. The adjoint method is a technique used to calculate the aerodynamic sensitivities efficiently in gradient-based optimization methods. The main strength of the adjoint method is that it keeps the cost of computing gradients the same, regardless of the number of design variables [14]. The adjoint method emerges within the optimal control field [15]. Then, the structural design field begins utilizing adjoint methods in structural optimization challenges [16]. Pironneau conducts the first study that benefited from the adjoint method in fluid problems. He uses the method to minimize drag in Stokes Flow [17]. Jameson significantly broadens the application of the method by employing it for aerodynamic optimization problems governed by Euler equations [18]. The method finds application in optimization problems involving the Navier-Stokes equations as well [19]. Later, the method is applied to various optimization problems of airfoil [20], wing [21], aircraft configurations [22], gas turbines [23], wind turbines [24], automotive [25], internal flow [26], fairing systems [27]. Also, the method is studied by ONERA and Airbus for three aerodynamic optimization challenges introduced by the AIAA Optimization Discussion Group in [28].

There are two main approaches to the adjoint method. These are the continuous ad-

joint and the discrete adjoint methods. The continuous adjoint approach is developed before the discrete one. In this approach, the partial differential equations are first linearized, and discretization occurs later. Therefore, the errors in gradient are highly dependent on the mesh size [29]. Moreover, manual differentiation of the partial differential equations is needed, which makes implementation of the method difficult. Also, the issues may originate from implementing boundary conditions and turbulence models as well [30]. However, this approach is recognized for its memory efficiency.

The latest studies of the adjoint methods utilize the discrete adjoint approach, which Elliot introduces in [31]. The primary difference of the method lies in deriving the adjoint equations from the discretized form of the partial differential equations. As a result, issues regarding the implementation of boundary conditions and turbulence models are not seen in this procedure. This approach has the advantage that gradients are not dependent on the mesh size compared to the continuous adjoint method, and the derivatives can be computed with automatic differentiation [32]. Automatic differentiation is a technique used to compute derivatives of subroutines and functionals within computer code [33]. Although automatic differentiation is not necessary, it offers substantial advantages, particularly when dealing with many design variables. Therefore, it is the standard in modern practice.

The adjoint method in aerodynamic shape optimization can utilize various geometry parametrization techniques, as demonstrated in the referenced paper [34]. These techniques include Bezier surface Free Form Deformation, B-Splines, Class Shape Transformation function, Hicks-Henne bump functions, Radial Basis Function, and Singular Value Decomposition method. These methods enable precise and controlled modifications to the geometry and enhance the efficiency of the optimization process.

1.3 Objectives and Outline of the Thesis

The objective of this thesis is to perform aerodynamic shape optimization on a specific component of the cruise missile called the inlet cover. To achieve this, the discrete adjoint method is employed by utilizing the SU2 software suite, which is an

open-source collection of tools designed for computational fluid dynamics and aerodynamic shape optimization. The primary objective is to reduce the drag of the inlet cover and increase its opening moment about the hinge axis. The objectives of the study can be listed as follows:

- To verify the SU2 flow solver for missile flows
- To use a gradient-based optimization framework based on the discrete adjoint method
- To employ a Free Form Deformation box for surface parametrization
- To perform a single-objective drag minimization of the inlet cover
- To perform a single-objective moment maximization of the inlet cover with drag constraint
- To perform a multi-objective optimization for minimizing the drag of the cover while simultaneously increasing the opening moment

The thesis consists of four chapters. In the next chapter, the aerodynamic shape optimization framework based on the adjoint method is presented. In Chapter 3, the verification and optimization case studies are presented and discussed in detail. Finally, the main conclusions derived from the study are stated in Chapter 4.

CHAPTER 2

METHODOLOGY

The chapter lays the groundwork for the aerodynamic shape optimization of the inlet cover addressed in this thesis. It provides the theoretical background of the flow solution, optimization techniques, and tools utilized in the study. Beginning with introducing computational fluid dynamics fundamentals and applying the SU2 flow solver and its finite volume methodology for solving the Reynolds-Averaged Navier-Stokes equations. Turbulence modeling, a critical aspect of accurately simulating turbulent flows, is described, emphasizing the SST and SA turbulence models. Transitioning to optimization techniques, the chapter explains gradient-based optimization methods, emphasizing the advantages of automatic differentiation. The discrete adjoint method takes center stage, providing insights into gradient computation and sensitivity analysis. Moreover, the chapter introduces the Free Form Deformation (FFD) box method as a versatile deformation technique. Finally, the Framework for Aerostructural Design Optimization (FADO), a robust framework for managing the optimization workflow, is introduced. With a balance of theory and practical tools, this chapter sets the stage for diving into aerodynamic shape optimization.

2.1 Flow Solution with SU2

The open-source flow solver SU2 is employed in this work to obtain turbulent flow solutions by solving the governing Reynolds-Averaged Navier-Stokes equations with the finite volume method. The flow domain is discretized with unstructured tetrahedral grids. The Navier Stokes equations, also known as the conservation equations for mass, momentum, and energy in their differential form, are expressed as follows

[35].

$$\frac{\partial U}{\partial t} + \nabla \cdot \bar{F}^c - \nabla \cdot \bar{F}^v - S = 0 \tag{2.1}$$

where S represents the source term, and the conserved variables U are defined as:

$$U = \{\rho, \rho\bar{v}, \rho E\}^\top \tag{2.2}$$

The convective fluxes are given by:

$$\bar{F}^c = \begin{Bmatrix} \rho\bar{v} \\ \rho\bar{v} \otimes \bar{v} + \bar{\bar{I}}p \\ \rho E\bar{v} + p\bar{v} \end{Bmatrix} \tag{2.3}$$

where ρ represents density, $\bar{v}$ denotes velocity, p stands for pressure, and E represents total energy. The viscous flux vector is given by:

$$\bar{F}^v = \begin{Bmatrix} \cdot \\ \bar{\bar{\tau}} \\ \bar{\bar{\tau}} \cdot \bar{v} + \kappa \nabla T \end{Bmatrix} \tag{2.4}$$

where $\bar{\bar{\tau}}$ represents the viscous stress tensor, κ denotes the thermal conductivity, and T is temperature. The expression of the viscous stress tensor is given as:

$$\bar{\bar{\tau}} = \mu \left(\nabla\bar{v} + \nabla\bar{v}^T \right) - \mu\frac{2}{3}\bar{\bar{I}}(\nabla \cdot \bar{v}) \tag{2.5}$$

where μ is the viscosity.

2.1.1 Turbulence Modelling

Turbulence models are mathematical formulations that aim to capture the effects of unpredictable fluctuations in turbulent flows. SU2 provides users with a choice between two turbulence models: the Shear-Stress Transport (SST) model and the Spalart-Allmaras (SA) model. Both methods rely on eddy-viscosity turbulence models, which rely on the Boussinesq hypothesis. It proposes a relationship between the Reynolds stress tensor and the mean flow properties [36]. The hypothesis assumes that the turbulent effects can be modeled by an additional viscosity term called turbulent viscosity.

The Spalart-Allmaras one equation model is a commonly used turbulence model in computational fluid dynamics, especially for external flows [37]. The model solves

a single transport equation for the eddy viscosity. It is computationally efficient and provides reasonable accuracy.

The Shear-Stress Transport turbulence model is a two-equation eddy-viscosity model developed to handle the limitations of existing models in predicting turbulence behavior, particularly in aerodynamics [38]. Designed as a combination of the k-epsilon model and the Wilcox k-omega model. In boundary layers, it utilizes the k-omega formulation for a better near-wall solution. It smoothly transitions to the k-epsilon formulation in the outer regions to eliminate freestream dependence.

Both models are used for validation purposes, and their performances are compared with each other to decide the turbulence model in the optimization study.

2.1.2 Solver Settings

The following solver settings are employed in the SU2 flow solver to ensure accurate and efficient computation of the turbulent flow solutions:

- **Convective Flux Scheme**: The Jameson-Schmidt-Turkel (JST) scheme is used.
- **Time Discretization**: The Euler Implicit method allows for larger time steps and improved computational efficiency
- **Linear Solver**: The Flexible Generalized Minimal Residual (FGMRES) method is chosen for solving large, sparse linear systems.
- **Spatial gradients**: Green-Gauss method for accurate gradient reconstruction is employed.
- **Slope Limiter**: The Venkatakrishnan slope limiter is applied to flow and turbulence equations, preventing unphysical oscillations.

These settings ensure robust and accurate simulation of turbulent flows, utilizing advanced numerical techniques.

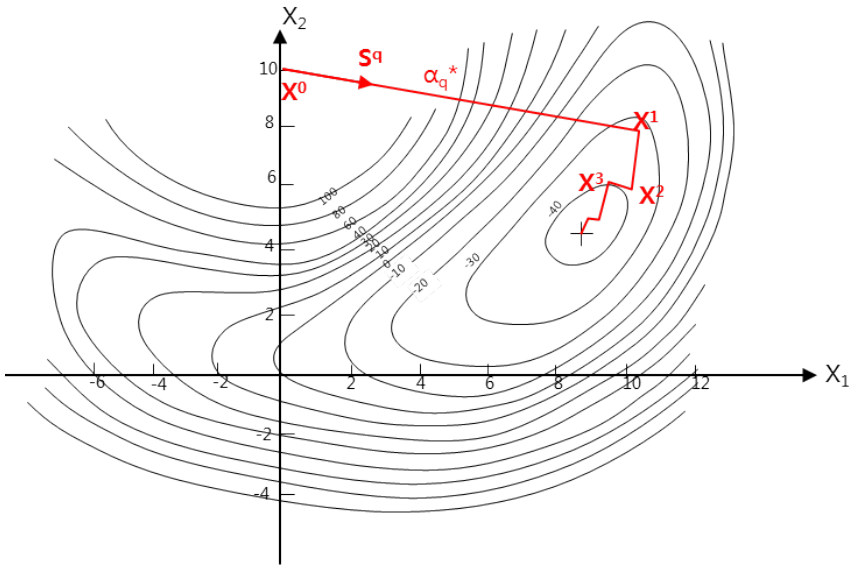

Figure 2.1: Illustration of Gradient-Based Optimization [41]

2.2 Gradient Based Optimization

Aerodynamic shape optimization is a complex task in the design process of aerial vehicles. Managing numerous design variables effectively to achieve desired aerodynamic performance goals is challenging. Gradient-based optimization is a widely recognized and efficient technique for aerodynamic shape optimization problems [39] [40]. The method benefits from a gradient vector to continuously enhance the design of aerodynamic components through iterative processes. Figure 2.1 demonstrates the application of gradient-based optimization techniques for an optimization task. Design variables are adjusted in alignment with the gradient direction to optimize a specific objective.

In computational modeling, computing derivatives accurately is central for sensitivity analysis. Various methods exist for this purpose. These include finite-difference methods, the complex-step method, symbolic differentiation, analytical methods, and algorithmic differentiation.

Finite difference methods are widely employed in computing derivatives because they are straightforward and easily applicable to many problems. They are described through equations derived from Taylor series expansions. The simplest form, known

as the forward difference formula, is expressed as:

$$\frac{\partial \boldsymbol{F}}{\partial x_j} = \frac{\boldsymbol{F}\left(\boldsymbol{x} + \boldsymbol{e}_j h\right) - \boldsymbol{F}(\boldsymbol{x})}{h} + \mathcal{O}(h) \tag{2.6}$$

where h is the step size, and $O(h)$ denotes the truncation error. While finite differences are easy to implement, their accuracy depends on the choice of step size. Decreasing h reduces truncation error. Moreover, as the number of design variables increases, the computational cost of evaluating the gradient vector also increases proportionally. This drawback challenges optimization problems with many design variables because computation cost is crucial for iterative optimization processes.

Symbolic differentiation and analytical methods typically involve manually deriving derivatives from mathematical equations. It requires a deep understanding of the governing equations and meticulous derivation of each term. However, these approaches can be error-prone, time-consuming, and unsuitable for practical problems. Moreover, dealing with complex turbulent Navier-Stokes equations involves assumptions that lead to inaccuracies in the gradients [29].

Automatic differentiation is an alternative approach for calculating gradient. It offers noteworthy advantages, especially in scenarios with many design variables [42]. This method targets computer codes directly and relies on the principle that a computer program, regardless of its complexity, comprises a series of basic arithmetic operations. The derivative of the input variables of the computer program can be calculated by differentiating these operations with the chain rule. Therefore, the new code version with reconstructed operations is created for computing gradient. The reconstructed version of the code is designed based on the computational graph of the calculations made by the program. An example of the computational graph for Equation 2.7 can be seen in Figure 2.2.

$$\mathrm{y} = \mathrm{f}\left(x_1, x_2\right) = \ln\left(x_1\right) + x_1 x_2 - \sin x_2 \tag{2.7}$$

There are two modes of automatic differentiation: forward and reverse modes. In the forward mode, computations are performed in the direction from inputs to outputs. On the other hand, in reverse mode, computations are performed in the reverse direction, from outputs to inputs [44]. Therefore, forward and reverse automatic dif-

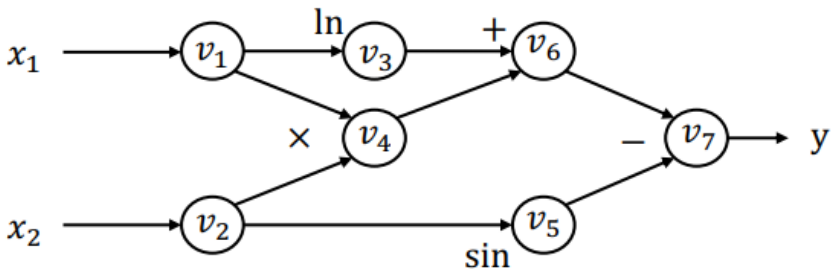

Figure 2.2: Example Computational Graph [43]

ferentiation modes require separate algorithms [45]. Due to their direction and intrinsic formulations, the forward mode is effective when dealing with a small number of inputs and a large number of outputs, whereas the reverse mode is effective when dealing with a large number of inputs and a small number of outputs. Therefore, the reverse mode is preferable for shape optimization problems with many design variables and relatively fewer outputs.

2.3 Discrete Adjoint Method

The discrete adjoint method is a powerful tool for the gradient computation of a function. The primal solution in this thesis is the solutions of the Navier Stokes equations, denoted as Equation 2.1. The discretized system of equations for design variable vector $\boldsymbol{x}$ are solved to find flow variable vector $\boldsymbol{w}$. The system of equations can be represented as follows:

$$\boldsymbol{R}(\boldsymbol{x}, \boldsymbol{w}) = 0 \tag{2.8}$$

where $\boldsymbol{R}$ represents the residual vector. The Equation 2.8 consists of conservation equations of mass, momentum, and energy as well as turbulence modeling equations written for each cell in the computational domain. Therefore, the size of the system of equations is equal to the number of the governing equation times the total number of cells. Iterative solution methods are employed to resolve the system of equations, thereby obtaining the flow variables represented by **w**. The scalar objective function of f can be written as:

$$f = f(\boldsymbol{x}, \boldsymbol{w}) \tag{2.9}$$

The computation of the objective function does not require any iteration and can be directly calculated with $\boldsymbol{x}$ and $\boldsymbol{w}$. Therefore, it is significantly less expensive than the flow solution. The total derivative of the design variable with respect to objective function can be expressed by chain rule as follows:

$$\underbrace{\frac{\mathrm{d}f}{\mathrm{d}\boldsymbol{x}}}_{1\times n_x} = \underbrace{\frac{\partial f}{\partial \boldsymbol{x}}}_{1\times n_x} + \underbrace{\frac{\partial f}{\partial \boldsymbol{w}}}_{1\times n_w}\underbrace{\frac{\mathrm{d}\boldsymbol{w}}{\mathrm{d}\boldsymbol{x}}}_{n_w\times n_x} \tag{2.10}$$

The partial derivatives of the f with respect to **x** and **w** are inexpensive because it does not require the solution of a system of equations and can be computed explicitly. $\frac{\partial f}{\partial \boldsymbol{x}}$ represents how the objective f changes when one component of the design vector $\boldsymbol{x}$ is changed while keeping the flow variables $\boldsymbol{w}$ constant. Similarly, $\frac{\partial f}{\partial \boldsymbol{w}}$ represents how objective f changes when one element of the flow variables $\boldsymbol{w}$ changes while keeping the design vector $\boldsymbol{x}$ constant. The calculation of $\frac{\mathrm{d}\boldsymbol{w}}{\mathrm{d}\boldsymbol{x}}$ is expensive because it needs the solution of Navier-Stokes equations.

Apparently, the $\frac{\mathrm{d}\boldsymbol{w}}{\mathrm{d}\boldsymbol{x}}$ is needed to calculate the total derivative of the objective function with respect to design variables. The partial derivative arises when the chain rule is applied to $\boldsymbol{R}$ as below. Note that $\frac{\partial \boldsymbol{R}}{\partial \boldsymbol{x}}$ needs to be zero to satisfy governing equations.

$$\frac{\mathrm{d}\boldsymbol{R}}{\mathrm{d}\boldsymbol{x}} = \frac{\partial \boldsymbol{R}}{\partial \boldsymbol{x}} + \frac{\partial \boldsymbol{R}}{\partial \boldsymbol{w}}\frac{\mathrm{d}\boldsymbol{w}}{\mathrm{d}\boldsymbol{x}} = 0 \tag{2.11}$$

The substutition of $\frac{\mathrm{d}\boldsymbol{w}}{\mathrm{d}\boldsymbol{x}}$ from Equation 2.11 to 2.10 results in:

$$\underbrace{\frac{\mathrm{d}f}{\mathrm{d}\boldsymbol{x}}}_{1\times n_x} = \underbrace{\frac{\partial f}{\partial \boldsymbol{x}}}_{1\times n_x} - \overbrace{\underbrace{\frac{\partial f}{\partial \boldsymbol{w}}}_{1\times n_w}\underbrace{\frac{\partial \boldsymbol{R}^{-1}}{\partial \boldsymbol{w}}}_{n_w\times n_w}}^{\boldsymbol{\psi}^T}\underbrace{\frac{\partial \boldsymbol{R}}{\partial \boldsymbol{x}}}_{n_w\times n_x} \tag{2.12}$$

where ψ represents the adjoint vector. It can be computed by solving the following linear system using iterative methods. Since the $\boldsymbol{x}$ does not appear in the following equation, the cost of the solution is independent of design variables.

$$\underbrace{\frac{\partial \boldsymbol{R}^T}{\partial \boldsymbol{w}}}_{n_w\times n_w}\underbrace{\boldsymbol{\psi}}_{n_w\times 1} = \underbrace{\frac{\partial f^T}{\partial \boldsymbol{w}}}_{n_w\times 1} \tag{2.13}$$

After the solution of the adjoint equations, the total derivative of the objective function can be computed as follows:

$$\frac{\mathrm{d}f}{\mathrm{d}\boldsymbol{x}} = \frac{\partial f}{\partial \boldsymbol{x}} - \boldsymbol{\psi}^T\frac{\partial \boldsymbol{R}}{\partial \boldsymbol{x}}. \tag{2.14}$$

In summary, the discrete adjoint method is applied by the following these steps :

1. Calculating the $\frac{\partial R}{\partial w}^T$ and $\frac{\partial f}{\partial w}^T$ explicitly.
2. Solution of the adjoint vector ψ from Equation 2.13
3. Calculating $\frac{\partial R}{\partial x}$ and $\frac{\partial f}{\partial x}$ explicitly.
4. Calculating the total derivative $\frac{df}{dx}$ from Equation 2.14

As derived and stated previously, it is important to stress that the computation cost of the solution of the adjoint equations is independent of the size of the design variable vector $\boldsymbol{x}$. This characteristic offers significant advantages for computing gradients in optimization problems governed by systems of equations, such as Navier-Stokes equations. This approach is also known as the adjoint method, and its computational cost is proportional to the number of objective functions. In other words, the linear system needs to be solved for each interest function. [29].

2.3.0.1 Evaluation of Surface Sensitivity Derivatives

After solving the adjoint equations, sensitivities of the objective function are obtained. These sensitivities represent the impact of perturbations at each node of the surface mesh on the objective function. To provide a concrete picture, the surface sensitivity distribution of the Onera M6 wing for the drag coefficient is given in Figure 2.3. These sensitivities are utilized for deforming the surface to achieve the design target. However, defining each node position as a design variable is unsuitable since it leads to excessive degree of motion. Therefore, a systematic approach to deformation is required to explore the design space adequately.

2.4 Free Form Deformation Box

Free Form Deformation (FFD) box is an efficient method for aerodynamics shape optimization problems [47]. FFD boxes can seamlessly handle both structured and unstructured CFD grids. It offers an alternative CAD-independent parametrization

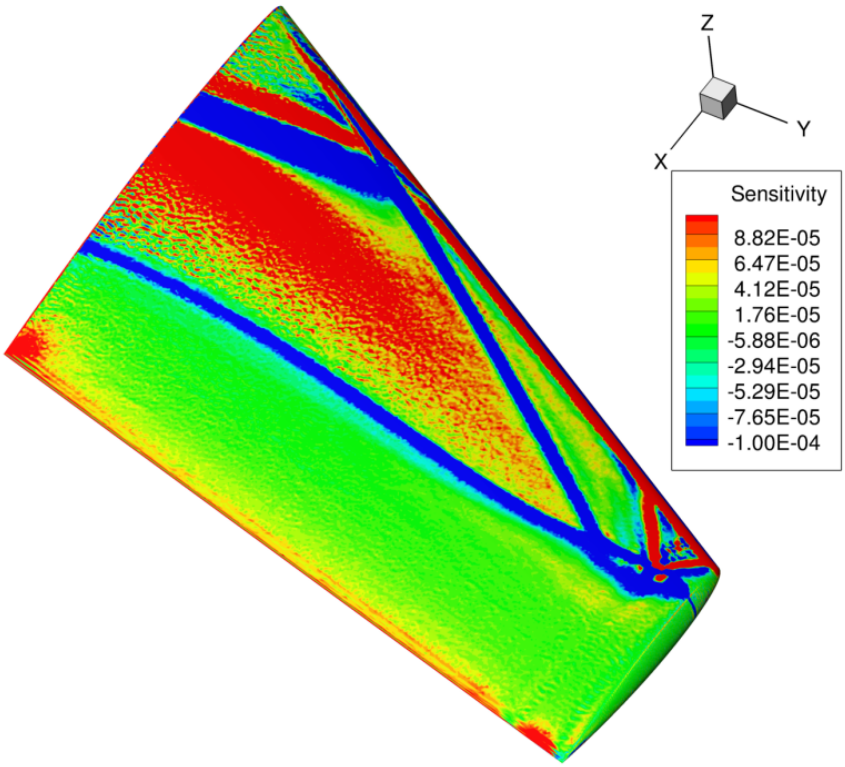

Figure 2.3: Drag Sensitivity of OneraM6 Wing [46]

technique directly applicable to the discretized computational grids. The adjustment of reducing the number of design variables while still maintaining precise control, flexibility, and freedom is vital for shape optimization. The FFD boxes consist of control points, also known as lattice points. The shape of the design surface is controlled by adjusting the positions of these lattice points of the FFD box. Each control point influences a specific surface region by affecting the nearby geometry. The control points make possible localized changes that collectively shape the whole surface [48]. An example of FFD Box and lattice points can be seen for a blended wing body configuration in Figure 2.4.

The FFD box, which surrounds the design surface, employs Bezier curves for deformation. The number of the lattice points determines the degree of the Bernstein polynomials used in this process. The parametrization equation, which describes deformation, is provided as follows:

$$X(u,v,w) = \sum_{i=0}^{l}\sum_{j=0}^{m}\sum_{k=0}^{n} P_{i,j,k} B_i^l(u) B_j^m(v) B_k^n(w) \tag{2.15}$$

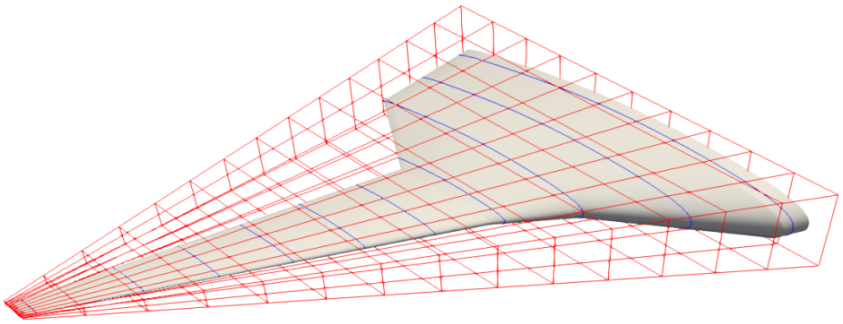

Figure 2.4: FFD Box over a Wing-Body Configuration [49]

where l, m, n denote the number of lattice points along each direction within the three-dimensional space and u, v, w represent the parameters of Bernstein polynomials, each ranging between 0 and 1. The P represents the coordinates of the lattice point indexed by i, j, and k. Finally, $B_i^l(u)$, $B_j^m(v)$, and $B_k^n(w)$ denote the Bernstein polynomials.

The coordinates of the surface nodes are converted into parametric coordinates of the Bernstein polynomials. Therefore, the position of the lattice points evolves into design variables, and they can control the design surface. After adjusting the lattice point position, the new coordinates of the surface nodes can be obtained by directly evaluating the mapping described in 2.15. This kind of parameterized control allows smooth deformation [50].

2.5 FADO: Framework for Aerostructural Design Optimization

The study conducted in this thesis focuses on adjoint-based shape optimization, which involves several elaborate steps. These include solving RANS equations and discrete adjoint equations, projecting surface sensitivities to design variables, mesh deformation, and applying robust optimization algorithms. Therefore, the framework plays a critical role in managing the input-output operations of these steps and navigating through these multifaceted processes. The SU2 software suit has a built-in shape optimization framework for conducting various optimization tasks. However, it is not utilized due to special requirements within the optimization problem, such as the need to bound each design variable separately and employ distinct solver controls

for RANS and adjoint equations. Instead, the Framework for Aerostructural Design Optimization (FADO) is utilized [51] .

FADO facilitates the execution of simulation codes, which use text files for inputs and outputs. The framework wraps the execution codes to make integrating these codes into optimization workflows easier, even if they don't have a user-friendly Python interface. Furthermore, different libraries and tools can be combined and operated together to leverage their individual strengths and functionalities. While scripting is still needed, the framework streamlines the manageability by enabling users to control the entire workflow within a single script. The framework comprises classes and modules designed to facilitate this streamlined approach, including:

- **InputVariable** class provides a structured approach to defining design variables, containing attributes such as initial values, bounds, and scaling factors, which are important for executing optimization algorithms towards optimal solutions.
- **Parameter** class handles extra settings important for optimization, like penalty factors or tuning parameters. It makes this process easier by allowing users to switch between predefined values and save them to files.
- **ExternalRun** class drives the execution of external commands and processes. The class creates a new process for each run and allows for lazy execution, meaning that a new process does not start until necessary. It manages copying and symbolic linking of data and configuration files to specified directories along with parameters and variables to the configuration files.
- **Objectives** class is a component designed to control objective-related information. It includes attributes such as the optimization type, which specifies whether the objective is minimization or maximization, the objective function scaling factor, and a weight associated with the objective for multiple objectives. These attributes collectively define the objective's role in the optimization process.
- **Constraints** class facilitates the addition and management of equality and inequality constraints by `addEquality`, `addLowerBound`, `addUpperBound`,

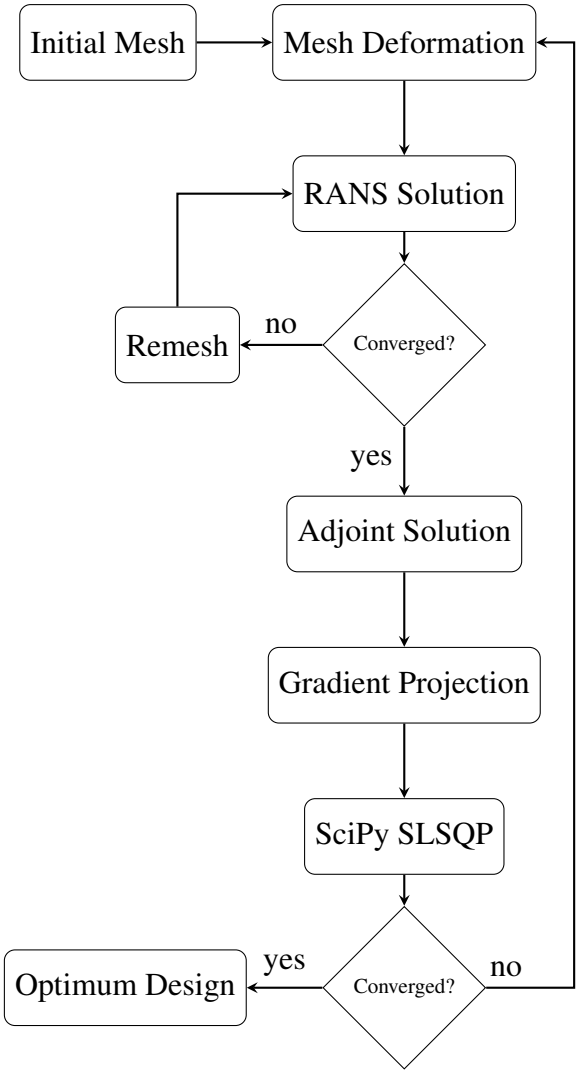

Figure 2.5: Optimization Process

and `addUpLowBound` attributes.

- **ScipyDriver** provides an interface between optimization problems and the SciPy [52] library's optimization algorithms like BFGS, COBYLA, and SLSQP. It enables the integration of these algorithms by feeding them with predefined objective and constraint function wrappers.

This study employs the SLSQP (Sequential Least Squares Quadratic Programming) optimization algorithm from the SciPy library. The optimization algorithm is widely used and exhibits considerable performance advantages in aerodynamic shape optimization problems, as Nagawkar documented [53].

The diagram in Figure 2.5 illustrates an iterative optimization process. Initially, Fluent Meshing, a commercial software, generates the initial mesh. Subsequently, the volume mesh, in CGNS format, is provided to the RANS solver called SU2_CFD. Sometimes, the solution may diverge due to low-quality cells resulting from mesh deformation. In such instances, the mesh is regenerated from an improved surface mesh to address divergence issues. Following this, the flow solution is fed into the discrete adjoint solver called SU2_CFD_AD. The adjoint solver obtains surface sensitivities by solving discrete adjoint equations, as Section 2.3 elaborates. Then, these sensitivities are projected to design variables by gradient projection software SU2_DOT_AD. The SLSQP optimization algorithm governs the optimization process by evaluating gradient, objective, and constraint functions. It selects an optimal step size and direction and updates the design vector accordingly. This procedure continues iteratively until convergence criteria are satisfied.

CHAPTER 3

RESULTS AND DISCUSSION

This chapter presents the results of the study and provides an in-depth discussion. It begins by selecting a suitable starting point for optimization studies, referred to as the baseline configuration. The baseline configuration is inspired by the design of the ÇAKIR [54] anti-ship cruise missile. Initially, the specifications, dimensions, and detailed components of the baseline configuration are introduced. The baseline configuration serves as the basis for subsequent analysis and optimization efforts.

Following this, attention shifts to choosing the optimization design condition. The design condition is selected by considering real-world operational scenarios. After that, verification studies for two experimental test cases are presented. These studies serve to verify the accuracy and reliability of the SU2 flow solver by comparing computational results with experimental data. Subsequently, a grid independence study for the baseline configuration is performed by using four different mesh resolutions. Moreover, this chapter investigates turbulence models integrated into the SU2 solver for selected grid resolutions.

Continuing, the chapter examines the parallel performance of the SU2 flow solver. The convergence pattern of the flow solution is also discussed. Subsequently, the chapter delves into the specifics of the FFD box, including its dimensions and placement, which are essential for conducting effective optimization. After, geometric constraints that shape and guide the search for optimal solutions are introduced.

Three optimization strategies are implemented. Firstly, a single objective drag minimization of the cover is pursued. Secondly, a single objective opening moment maximization of the cover with drag constraint is targeted. Finally, multi-objective opti-

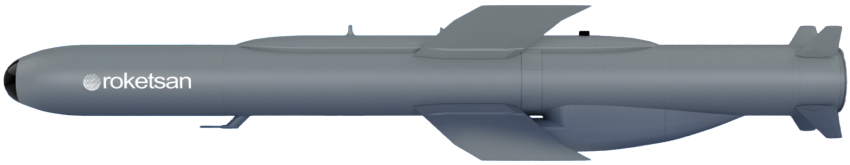

Figure 3.1: ÇAKIR Cruise Missile [54]

mizations with weight factors are performed to address different optimization objectives. Through these strategies, the aim is to enhance the aerodynamic performance of the cover across different optimization criteria.

3.1 Baseline Configuration

In optimization studies, selecting the appropriate baseline configuration is important for accurately evaluating the performance of the study. The baseline configuration employed in this thesis is inspired by the ÇAKIR [54] cruise missile designed by Roketsan Missiles Inc. The missile is capable of being launched from multiple platforms like UCAVs, fighter jets, and naval vessels. It offers a range exceeding 150 kilometers and is equipped with the KTJ-1750 turbojet engine [54]. The illustration of the missile is given in Figure 3.1

Most basic geometries are preferred for the baseline configuration, including a hemisphere for the nose and a cylinder for the fuselage. As previously stated, the sizing of the baseline resembles the sizing of the ÇAKIR missile. Therefore, the hemisphere cylinder with 300 mm in diameter and 3000 mm in length is chosen for baseline configuration. The pitot-type inlet is employed, and it has a semicircular capture area with 170 mm diameter. The inlet is positioned such that the capture area is located at the midpoint of the missile, which is a 1500 mm distance behind the tip of the nose. The side view of the baseline configuration can be seen in Figure 3.2.

The reference length corresponds to the diameter of the missile, measuring 0.3 meters. Similarly, the reference area is defined as the cross-sectional area of the fuselage, which is 0.070686 square meters. The internal flow that enters into the inlet does not exist in this study because the optimization problem focuses on the configuration with the cover installed. However, to provide a clearer understanding of the geometry, the

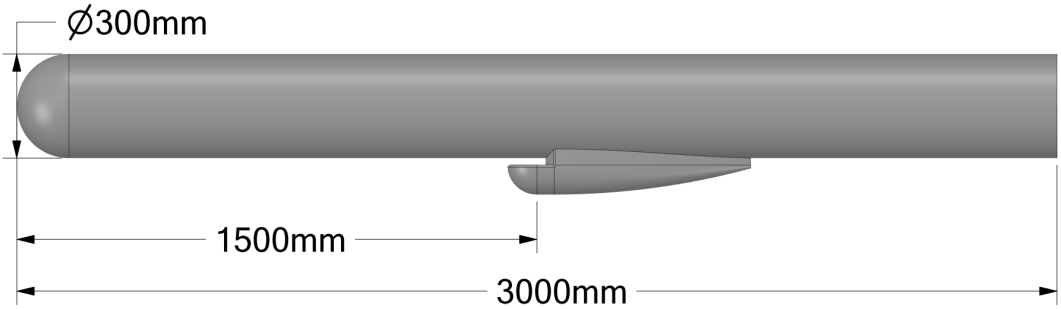

Figure 3.2: Baseline Configuration

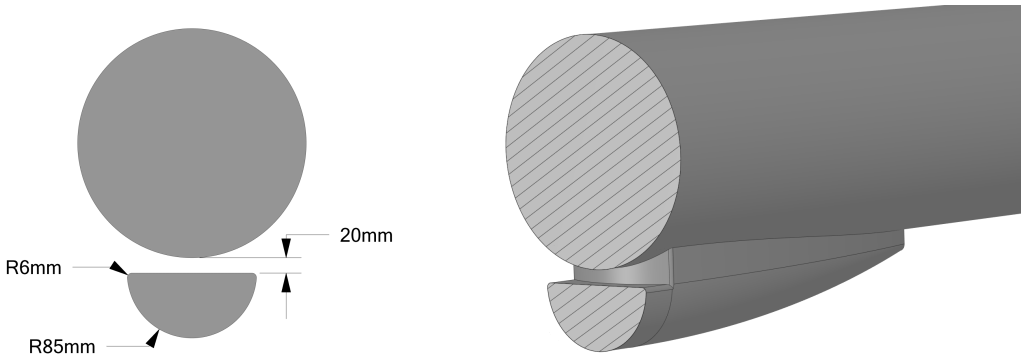

Figure 3.3: Cross Sectional View of the Inlet Cover

cross-section at the location of the capture area is illustrated in Figure in 3.3.

The capture area has a radius of 85 mm and fillets at each corner with a 6mm radius. The minimum distance between the inlet and the missile fuselage is 20 mm. The purpose of this space is to take clear air into the inlet and prevent the entry of the boundary layer produced by missile fuselage. The value of this distance is determined by an approximation of the boundary layer thickness at the location of the capture area. The following theoretical formulation that gives boundary layer thickness for incompressible flow over a flat plate is utilized [55].

$$\delta = \frac{0.37x}{\mathrm{Re}_x^{1/5}} \tag{3.1}$$

where δ is the boundary layer thickness, x is the distance from the flat plate leading edge, and Re_x is the Reynolds number based on distance x. For the baseline configuration which is inspired by the sea-skimming naval cruise missile Re_x can be computed at sea level altitude and 0.75 Mach number. The capture area has a distance

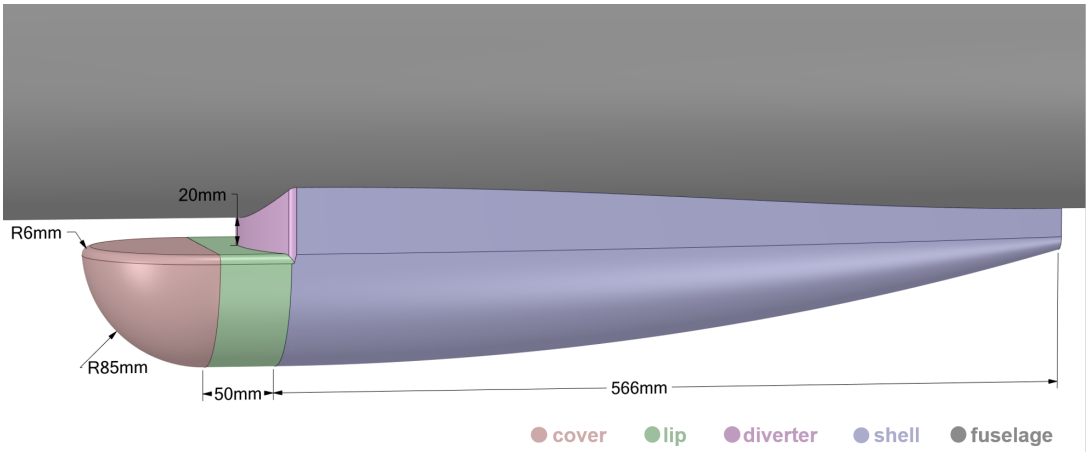

Figure 3.4: Components of Baseline Inlet Cover Configuration

of 1.5 meters from the tip of the nose. With the provided parameters, the boundary layer thickness δ computed as 18.3 mm. Therefore, with the safety margin diverter with 20 mm height is used in the baseline configuration.

There are four components that constitute the inlet assembly. Each of them is presented in a distinct color in Figure 3.4. In this study, the inlet cover is the design surface. Then, there is a component lip that has the capture area and takes the flow to the internal duct after the cover is jettisoned. The convex-shaped circular diverter separates flow into two sides. The diverter has a radius of 157 mm, a width of 170 mm, and a height of 20 mm, and it is positioned perpendicular to both the fuselage and the lip. The last component is a streamlined body called a shell. The shell geometry is taken from a widely used experimental test case and scaled. The model is known as the inlet-A [56]

3.2 Design Condition

The optimization design condition should be chosen close to the flight condition in which the missile configuration is exposed while gliding with the cover. An example operational plan serves as a reference point for determining optimization design conditions. It is assumed that a naval cruise missile featuring an inlet cover carried by a UCAV which cruises at 10 km altitude and 0.3 Mach number. For instance, the Bayraktar Akıncı is suitable for such operations [57]. The operational envelope of

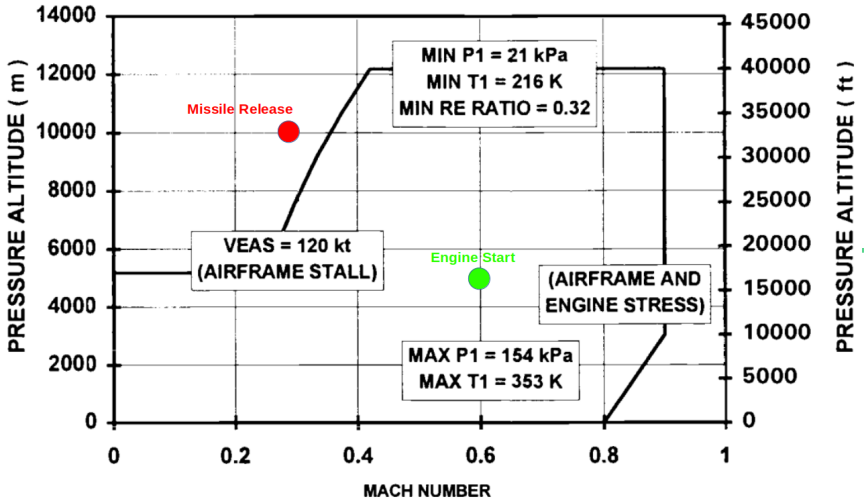

Figure 3.5: Operational Envelope of a Subsonic Airbreathing Missile [58]

Table 3.1: Design Condition

Altitude [m]	Pressure [Pa]	Temperature [K]	Mach Number	Reynolds Number
5000	54048	256	0.6	2.6×10^6

subsonic airbreathing missiles is given in Figure 3.5 [58].

It can be seen that the flight condition when the missile is launched from the platform falls outside of this envelope. Therefore, the gas turbine engine cannot be started in the release condition. The missile glides until a certain speed and the necessary flight conditions are met. The gliding also extends the range of the missile. To remain in a safe area, a region inside the envelope, which is 5 km altitude and 0.6 Mach number, is selected for the engine ignition and cover ejection point. Since the cover will separate from the missile at this point, selecting this point as the optimization design condition is reasonable. This way, the opening moment will be calculated and optimized under the correct flight conditions. The details of the flight conditions where the optimization takes place are given in Table 3.1

3.3 Verification Studies

Verification of the flow solver is an essential step before a design optimization process. In this section, the verification studies are presented. Two experimental test cases are utilized to verify the SU2 flow solver, and proper grid densities are selected.

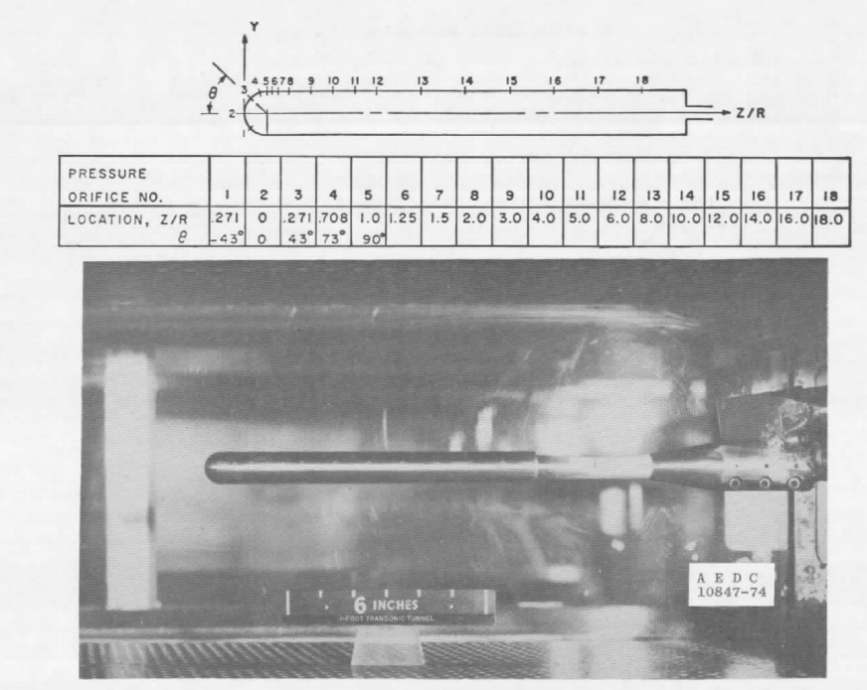

Figure 3.6: Wind Tunnel Model for Hemisphere Cylinder [59]

For both cases, the study is conducted under the flight conditions of 0.6 Mach number, which matches the design condition selected in Section 3.2.

The first case involves an experimental study examining the pressure distribution over a hemispherical cylinder body [59]. This study is particularly relevant because the baseline inlet cover and nose also have a spherical shape.

The second case investigates the aerodynamic coefficients of a missile configuration at various angles of attack [60]. The case is selected to demonstrate the solver's accuracy in finding aerodynamic forces and moments of missile configurations.

3.3.1 Hemisphere Cylinder Test Case

This study examines how airflow behaves around a hemisphere cylinder by testing in a wind tunnel [59]. The interest in the study stems from its relevance to improving the aerodynamic performance of missiles. This reference is valuable for verifying the SU2 flow solver because the baseline configuration in the optimization problem includes spherical shapes. The flight conditions used for the verification of the solver are given in Table 3.2.

Table 3.2: Test Condition for the Hemisphere Cylinder

Mach Number	**Reynolds Number**
0.6	3.25×10^5

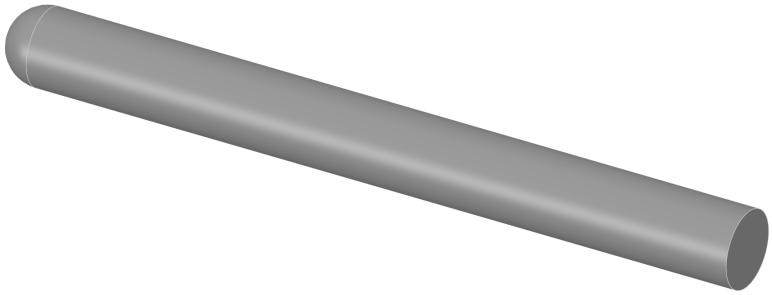

Figure 3.7: Hemisphere Cylinder Model

The Reynolds number calculation employs the diameter of the hemisphere cylinder as the reference length. Figure 3.6 shows the experimental setup used in the wind tunnel.

The eighteen pressure orifices on the surface of the model measure the static pressure along the Z direction. This experimental measurement is used to compare the results obtained from the SU2 flow solver. The model has 1 inch of diameter and 10 inches of length. The geometry is rather simple, and the solid model can be seen in Figure 3.7.

4 grids with varying cell sizes are used to perform a grid convergence study. The study is performed under a specific flight condition, which is 0.6 Mach number and zero degree of an angle of attack. The grids with the corresponding total number of cells and surface cells are given in Table 3.3.

The body of influence region that encapsulates the hemisphere cylinder surface and the base region behind the body is utilized to adjust grid sizes. All grids have twenty layers of prism cells. The first layer height is selected to ensure that the y^+ value is

Table 3.3: Grid Data for the Hemisphere Cylinder

Grid Name	Coarse	Medium	Fine	Finest
Number of Cells	1.07×10^6	2.48×10^6	7.50×10^6	13.06×10^6
Number of Surface Cells	3.06×10^3	1.20×10^4	4.81×10^4	8.52×10^4

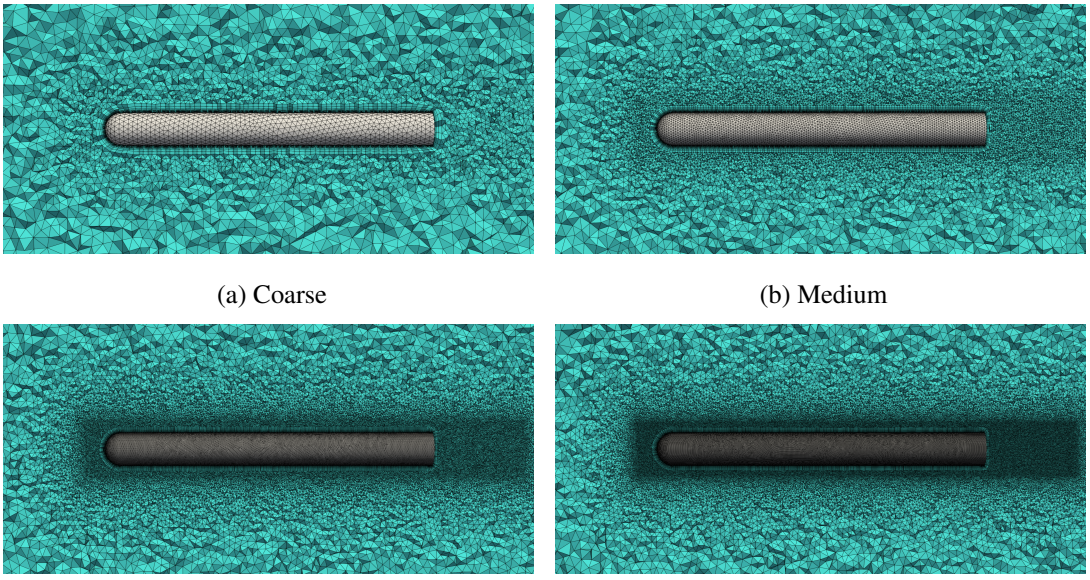

(a) Coarse

(b) Medium

(c) Fine

(d) Finest

Figure 3.8: Grid Independence Study for Hemisphere Cylinder

near one. This implies that the resolution of the boundary layer mesh is sufficient to capture the viscous sublayer. Two different methods are used to generate the prism layers. A geometric growth factor of 1.15 is used for the first ten layers. Then, in the second group of prism layers, the last ratio method is used to provide a smooth transition between prism layers and tetrahedral cells in the flow domain. The surface and the volume mesh at the symmetry plane of the flow domain can be seen in Figure 3.8.

A grid independence study is conducted using the SST turbulence model. The pressure distribution is plotted against the ratio of the Z coordinate to the radius of the body in Figure 3.9. This ratio indicates how the pressure changes along the surface of the body relative to its size. The pressure distribution is not provided for the entire nose length, which spans Z/R values between 0 and 7. The reason is that beyond the Z/R equals of 1.8, the pressure coefficients are predicted the same with all the

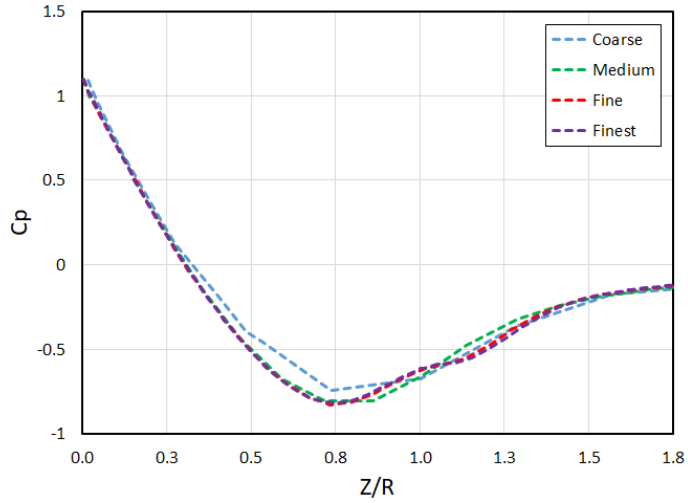

Figure 3.9: Surface Pressure Distribution along the Hemisphere Cylinder

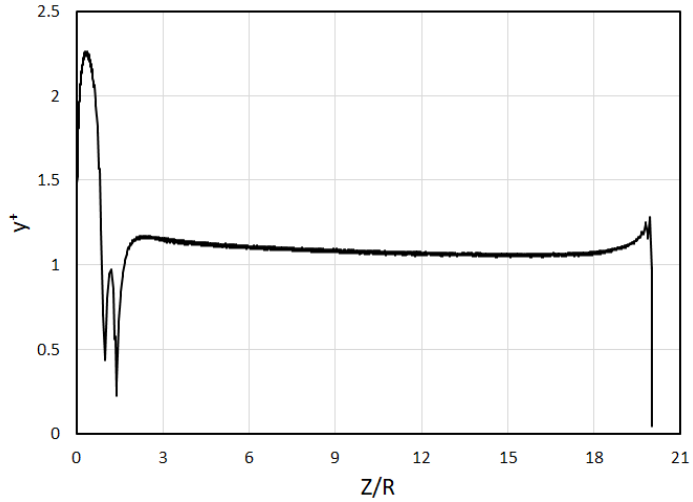

Figure 3.10: Variation of y^+ along the Hemisphere Cylinder for Fine Grid

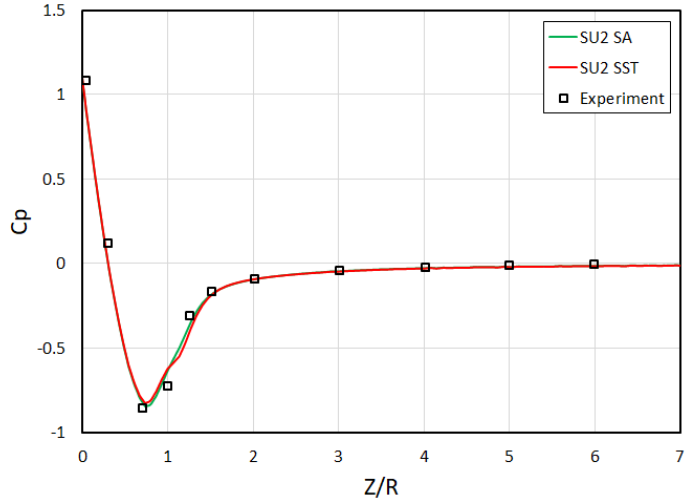

Figure 3.11: Surface Pressure Distribution along the Hemisphere Cylinder for Fine Grid

grids, which makes it challenging to distinguish the differences. Therefore, the focus is placed on the region where variations are observed. It can be seen that there is a change in the pressure distribution from the coarse to the medium and the medium to the fine meshes. However, the predictions with the fine and the finest meshes are about the same. This indicates that the fine mesh resolution provides a mesh-independent solution.

y^+ values for the fine mesh with respect to the Z direction are given in Figure 3.10. It can be seen that up to Z/R equal to 2, which corresponds to the region where the nose exists, the y^+ values oscillate; however, beyond that, the values are around one, indicating that the boundary layer mesh resolution is sufficient to capture the velocity gradient near the wall.

The SU2 flow solution is obtained using the SA and SST turbulence models for a fine mesh. The comparison with experimental results can be seen in Figure 3.11. The predictions of the SA and the SST turbulence models are very similar, with only a slight deviation noticeable near a point close to Z/R of 1.25. They also demonstrate strong consistency with the experimental data.

This case shows that the SU2 flow solver can accurately predict the pressure distribution along the hemisphere cylinder bodies with both SA and SST turbulence models. Therefore, it is a suitable tool for the optimization study.

3.3.2 NASA TM X-3070 Missile Test Case

In this case [60], the wind tunnel testing of an air-to-air missile conducted in the Langley 8-foot transonic pressure tunnel is considered. The aerodynamic coefficients obtained at 0.6 Mach number and various angles of attack are used in the verification study. The test conditions are given in Table 3.4.

Table 3.4: Test Condition for NASA TM X-3070 Missile

Mach Number	**Reynolds Number**	**Stagnation Temperature [K]**
0.6	2.77×10^5	332

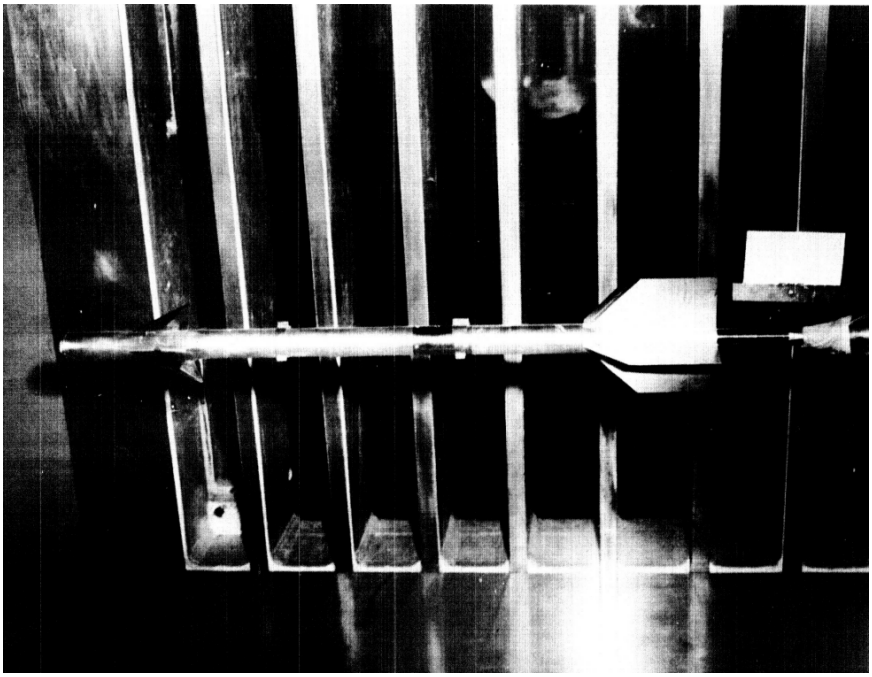

Figure 3.12: Wind Tunnel Model for NASA TM X-3070 Missile [60]

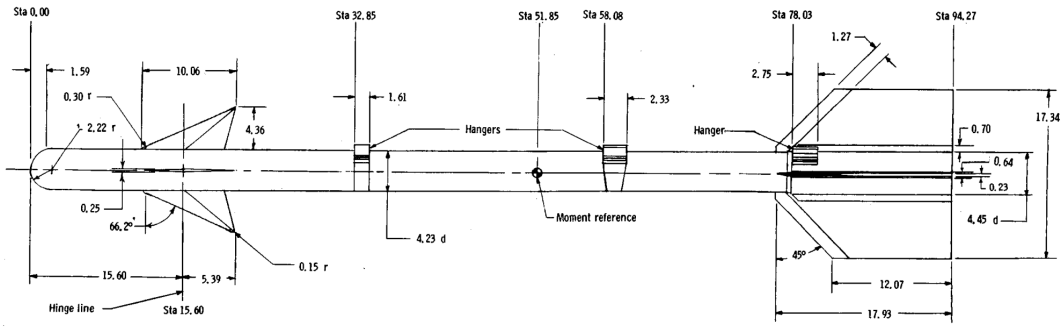

Figure 3.13: Technical Drawing of NASA TM X-3070 Missile [60]

A six-component electrical strain-gage balance is used to measure aerodynamic forces and moments. The measurement device inside the model is attached to a support system called a sting. A photograph of the model used in wind tunnel testing can be seen in Figure 3.12. The cruciform air-to-air missile has a fineness ratio of 22. It has a hemispherical nose and a cylindrical fuselage. The diameter of the aft fuselage increased by 17 percent due to the attachment of the tails. While the canard has a wedge shape and triangular planform, the tail has a trapezoidal planform. The detailed technical illustration of the model can be seen in Figure 3.13

The solid model of the missile is created by the software SpaceClaim and can be seen

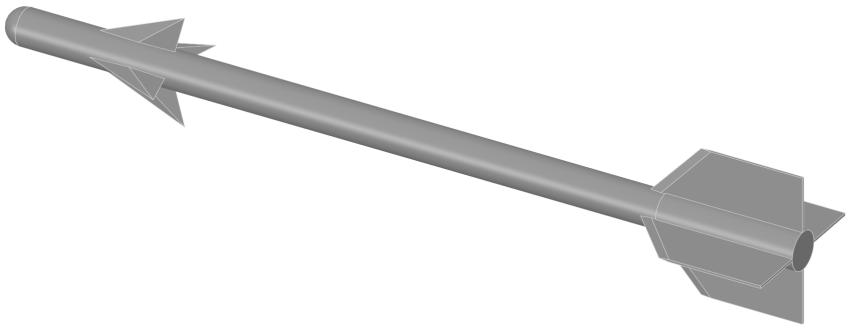

Figure 3.14: Solid Model for NASA TM X-3070 Missile

Table 3.5: Grid Data for NASA TM X-3070 Missile

Grid Name	Coarse	Medium	Fine	Finest
Number of Cells	1.08×10^6	3.73×10^6	8.65×10^6	1.8×10^7
Number Surface Cells	1.57×10^4	6.21×10^4	2.02×10^5	4.67×10^5

in Figure 3.14. Hangers on the configuration are not included in the solid model due to insufficient information regarding their shape and size. It is assumed that their impact on aerodynamic coefficients can be neglected. Selecting the appropriate grid size is crucial for capturing flow details directly affecting our area of interest. In this case, it is the aerodynamic coefficients. The grid size also affects the computation time of the analysis. Therefore, the grid independence study is conducted to determine the grid size that achieves a balance between accuracy and computational efficiency. The study is conducted with four grids of varying sizes. Surface cell sizes are adjusted to produce grids of differing resolutions. The study is carried out under a single flight condition at a Mach number of 0.6 and an angle of attack of 4.12 degrees. The grid with the corresponding total number of cells and surface cells are given in Table 3.5.

The surface and the volume mesh at a cross-section of the flow domain can be seen in Figure 3.15. A local base area refinement is employed to capture the wake region behind the missile. It is particularly important to compute the drag accurately. Also, the mesh of the nose and the edges of the fins are refined compared to the missile fuselage.

The drag coefficient with respect to the number of cells can be seen in Figure 3.15e. It can be seen that as the number of cells increases, the drag coefficient decreases.

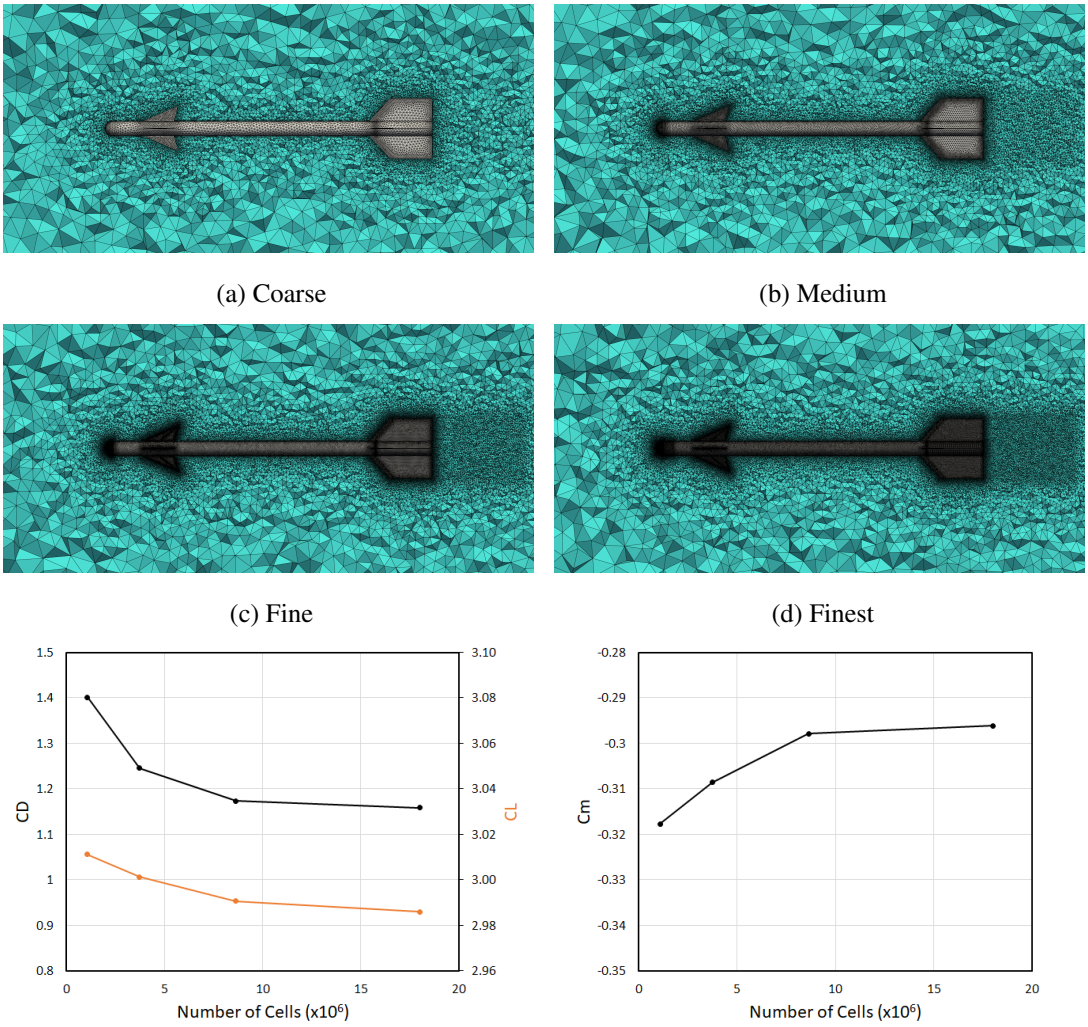

(a) Coarse

(b) Medium

(c) Fine

(d) Finest

(e) Drag and Lift Coefficient

(f) Moment Coefficient

Figure 3.15: Grid Independence Study for NASA TM X-3070 Missile

However, the amount of change in the drag coefficient decreases as the number of cells increases. Therefore, convergence to a constant value is observed for the fine and finest grids.

The lift coefficient with respect to the number of cells can be seen in Figure 3.15e. It is important to emphasize that the difference between a coarse mesh and a finest mesh is less than 1 percent. Therefore, it can be said that the results are independent of mesh for lift coefficient. Furthermore, it is notable that the convergence behavior still exists.

The pitching moment coefficient about the moment center with respect to the number

of cells can be seen in Figure 3.15f. The values are negative, which means the missile has a pitch-down moment. The magnitude of the moment coefficient decreases as the number of cells increases. Similar to the drag coefficient, the values converge to a constant value from the fine mesh onward.

When Figure 3.15 is evaluated, it is observed that the choice of mesh resolution affects the computed aerodynamics coefficients, including drag, lift, and pitching moment. However, it is practical to choose fine mesh since further refinement does not significantly improve results.

The experimental results are compared with fine mesh across a range of angles of attacks, spanning from -5 to 20 degrees. The comparison of the drag coefficient between the analysis and experiment is given in Figure 3.16. Remarkably, the results exhibit a high degree of agreement, demonstrating the same pattern across the entire range. From the graph, it can be observed that the drag coefficient remains around 1 within the range of -5 to 5 degrees. However, beyond 5 degrees, there is an abrupt increase in the drag coefficient.

The comparison of the lift coefficient between the analysis and experiment is given in Figure 3.17. The results are very close to each other and show the same pattern. There is a slight difference at 19.24 degrees, but the difference is minimal, and it is less than one percent. Moreover, the behavior of the lift coefficient with respect to the angle of attack is linear.

The comparison of the pitching moment coefficient about the moment center between the analysis and experiment is given in Figure 3.18. Within the range of -5 to 0.94 degrees, the results of the analysis are in good agreement with experimental data. A slight deviation becomes apparent after 2 degrees. However, the results of the analysis still exhibit the same pattern as the experimental data.

In conclusion, the SU2 flow solver has proven its ability to calculate aerodynamic coefficients for a generic missile configuration accurately. It is supported by comparing the SU2 analysis with experimental data over various angles of attacks between -5 and 20 degrees. This shows that SU2 is a convenient tool for calculating the aerodynamic coefficient of missile configurations, such as those featuring hemisphere noses

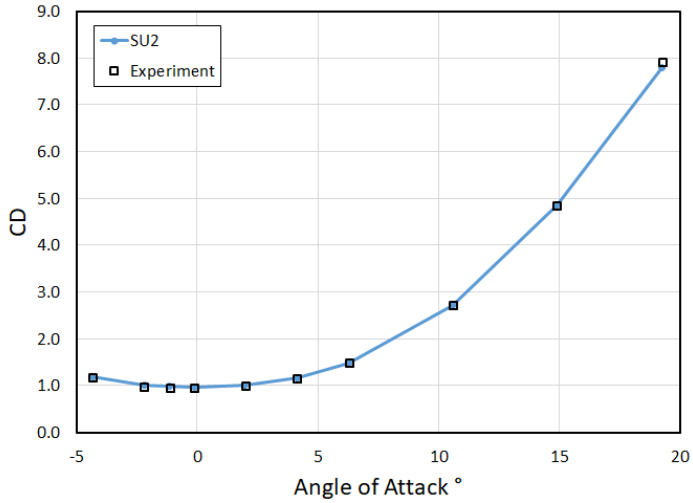

Figure 3.16: Variation of Drag Coefficient

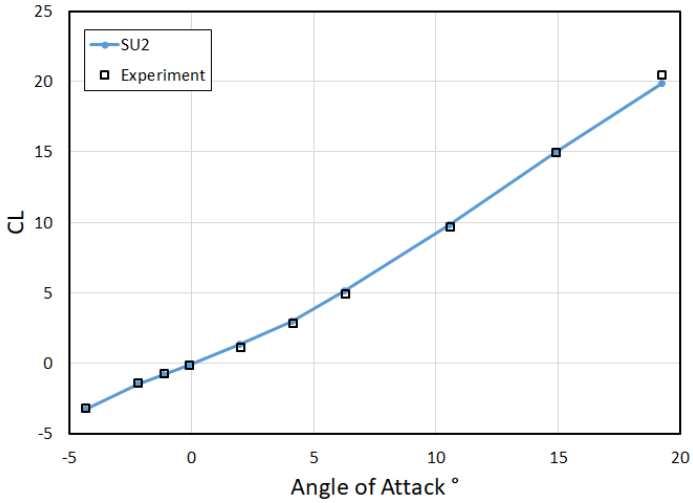

Figure 3.17: Variation of the Lift Coefficient

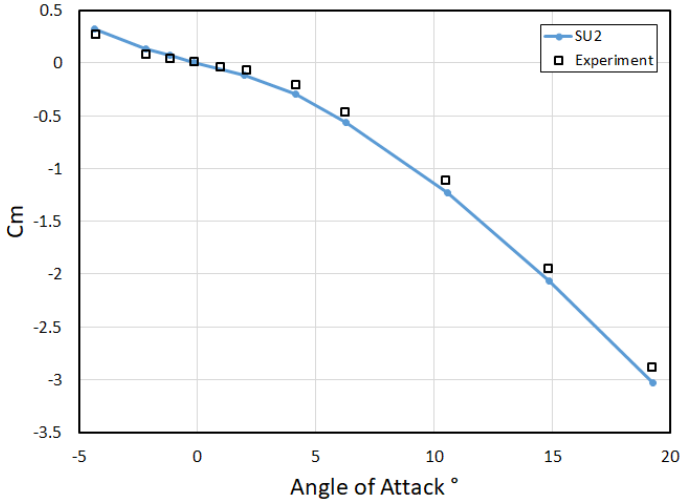

Figure 3.18: Variation of the Moment Coefficient

and cylindrical fuselages, like the baseline configuration studied in this thesis.

3.4 Grid Independence Study for the Baseline Configuration

Before proceeding with the optimization study, a grid independence study is conducted. It is crucial to discretize the solution domain finely enough to compute the aerodynamic coefficients accurately. However, using an excessively fine mesh increases the total number of cells, resulting in longer computation times. This is undesirable since it extends the duration of the analysis and optimization. The study uses four grids of different sizes. Surface cell sizes are adjusted to create grids with varying resolutions. All meshes consist of twenty layers of prism cells. The first layer height is chosen to maintain a y+ value near one. Two methods are employed to generate the prism layers. A geometric growth factor of 1.15 is applied for the first ten layers. Subsequently, the last ratio method is used for the remaining prism layers to ensure a smooth transition between the prism layers and the tetrahedral cells in the flow domain. The grids and the corresponding number of cells, and surface cells are given in Table 3.6.

The surface and volume meshes for the baseline configuration at the symmetry plane of the flow domain are illustrated in Figure 3.19. Compared to the fuselage, the mesh size of the nose, inlet parts, and particularly the inlet cover are refined.

The drag coefficient of the overall configuration and the inlet cover with different grids are displayed in Figure 3.20. Both of them exhibit a similar pattern. From the coarse to the medium mesh, the drag coefficient experiences a sharp decrease, followed by an increase from the medium to the fine meshes. The variations between the fine and the finest meshes are less pronounced than those seen in the earlier mesh levels. The difference in C_D between the fine and finest meshes is 0.48%, and for CD_{cover}, it is 0.42%.

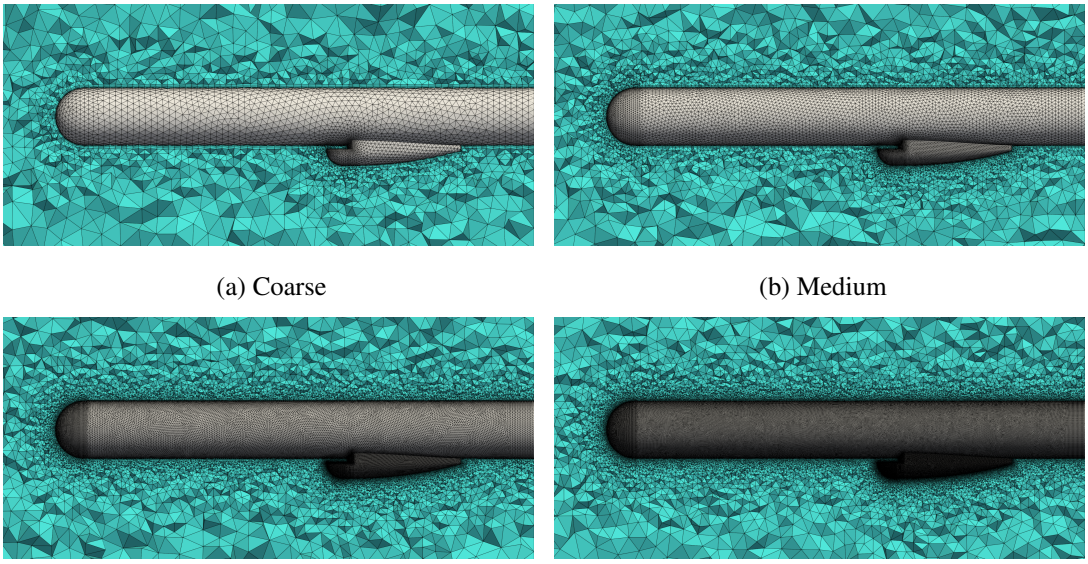

(a) Coarse (b) Medium

(c) Fine (d) Finest

Figure 3.19: Grid Independence Study for Baseline Configuration

Table 3.6: Grid Data for Baseline Configuration

Grid Name	Coarse	Medium	Fine	Finest
Number of Cells	8.90×10^5	2.10×10^6	4.62×10^6	1.00×10^7
Number of Surface Cells	2.38×10^4	6.08×10^4	1.38×10^5	3.08×10^5

The lift coefficient of the overall configuration and the cover with different meshes are plotted in Figure 3.21. CL decreases from coarse to medium meshes, and then it increases with the cell number. The maximum difference in CL is between the medium and finest meshes, and the difference is less than two percent. On the other hand, CL_{cover} rises with an increase in the cell number. The values of CL_{cover} for fine and finest meshes are almost the same.

The moment of the cover with respect to the hinge axis is plotted against the number of cells in Figure 3.22. While the change between coarse and medium meshes is abrupt, the differences between fine and finest meshes are negligible.

When evaluating Figure 3.20, 3.21 and 3.22, the choice of mesh resolution affects the computed aerodynamic coefficients, including the overall configuration drag and lift, as well as the cover's lift, drag, and opening moment. However, opting for a fine

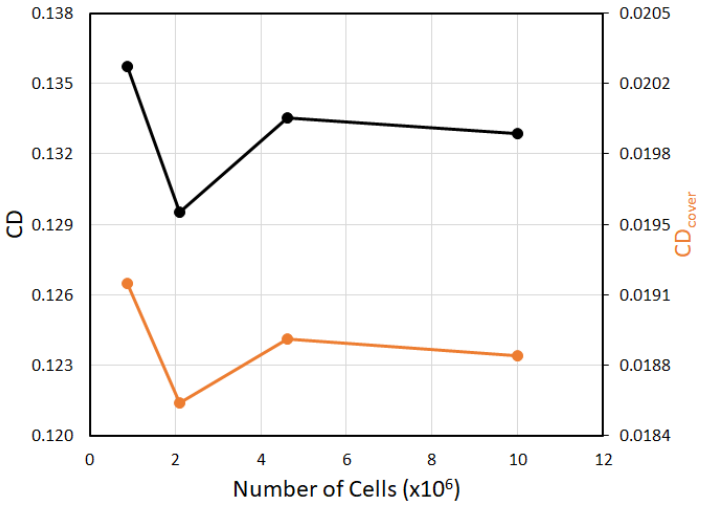

Figure 3.20: Drag Coefficient

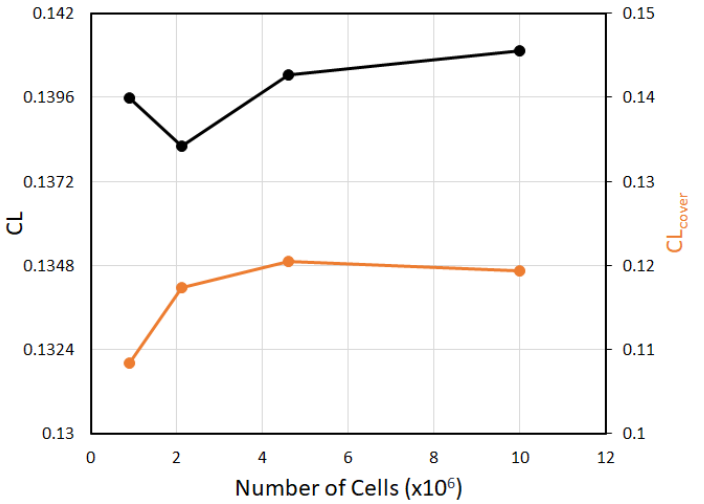

Figure 3.21: Lift Coefficient

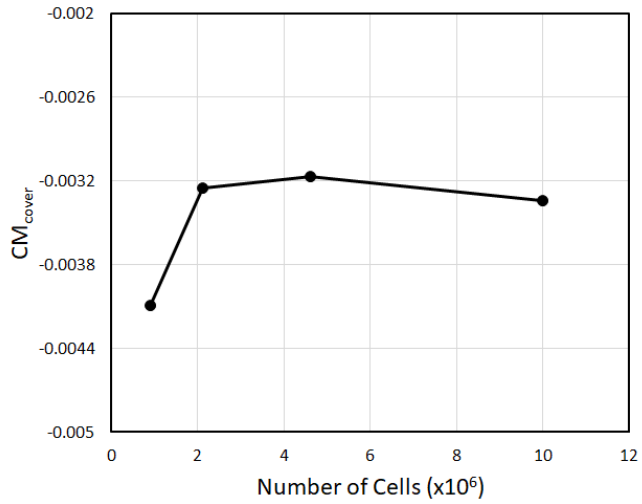

Figure 3.22: Moment Coefficient

Figure 3.23: Front View of the Surface Mesh for the Baseline Configuration

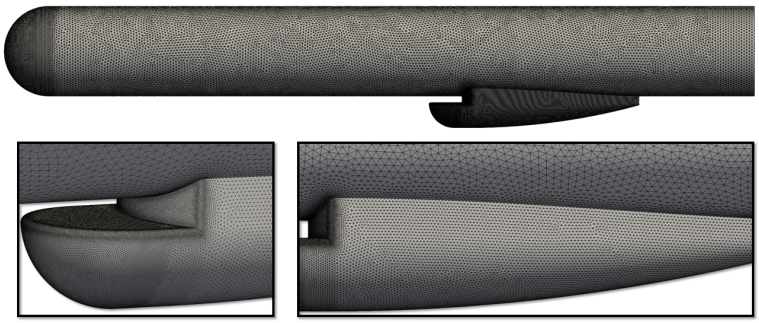

Figure 3.24: Side View of the Surface Mesh for the Baseline Configuration

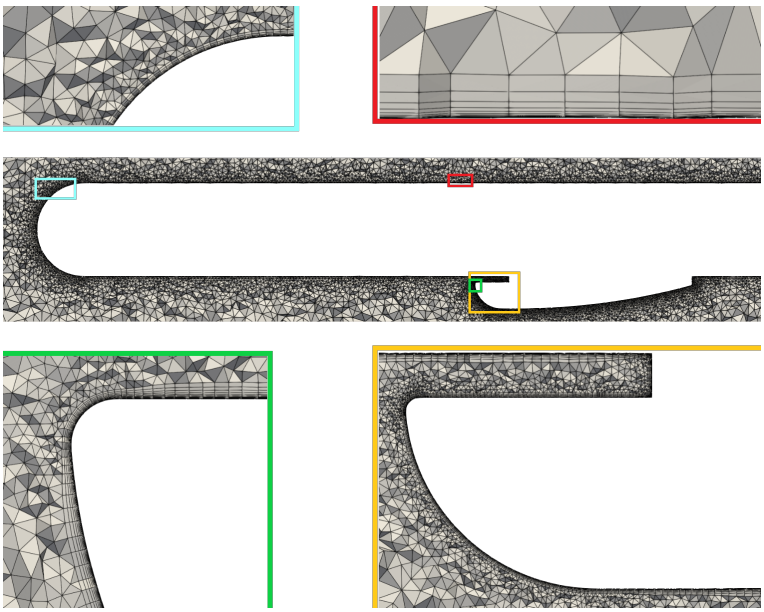

Figure 3.25: Cross-Section of the Volume Mesh for the Baseline Configuration

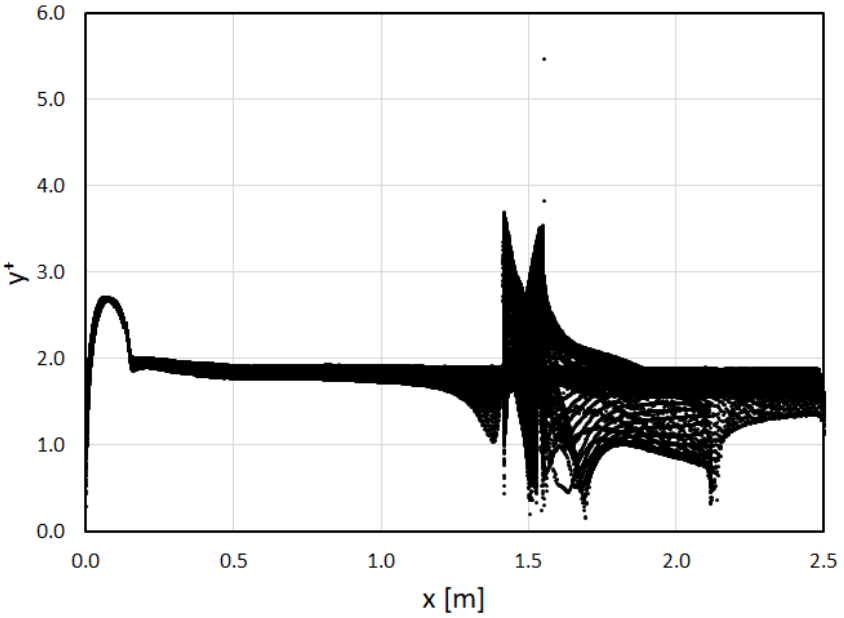

Figure 3.26: Variation of y^+ along Baseline Configuration

mesh is practical since further refinement does not significantly improve results. The detailed illustrations of the fine mesh are presented in Figure 3.23, 3.24 and 3.25.

The grid independence study is conducted using the SST turbulence model. The y+ values for the fine mesh are presented in Figure 3.26. It can be observed that the values are close to 1, but deviations exist around the nose and inlet components.

Comparison of the SST and SA turbulence models are compared with the fine mesh. The results are given in Table 3.7. The absolute values of the aerodynamic coefficients are greater in the SST model than in the SA model. The largest percentage difference is noted in C_D, with a value of 2.26%, while the smallest percentage difference is found in CL_{cover}, with a value of 0.85%.

Table 3.7: Turbulence Model Predictions

	C_D	CL	CD_{cover}	CL_{cover}	CM_{cover}
SST	0.1335	0.1402	0.0188	0.1204	-0.00317
SA	0.1305	0.1376	0.0186	0.1194	-0.00311
% Difference	2.26	1.87	1.48	0.85	1.69

3.5 Parallel Performance of the SU2 Flow Solver

The parallel performance of the SU2 flow solver is presented in Figure 3.27. The flow solution for the baseline configuration is computed with a geometrically increasing number of processors to generate the speed-up graph. It can be said that the parallel performance of the SU2 solver is close to the ideal speed-up until 32 processors. After that, it can be observed that the performance slightly deviates from the linear behavior.

The flow solution consists of 500 iterations. Figure 3.28 shows the residual behavior of the flow solution along the iterations. As the iteration number increases, the residuals of the conservative flow variables decrease. This indicates that the changes in flow variables diminish as the iteration number increases.

To assess the convergence of the analysis, it is meaningful to observe the fields of interest, which in this thesis are the aerodynamic coefficients. Figure 3.29 presents the values of CL and C_D for the baseline configuration with respect to iterations, It is observed that aerodynamic coefficients converge around iteration 200, after which they remain constant.

3.6 Aerodynamic Shape Optimization Studies

In order to enhance the aerodynamic performance of the engine inlet cover, single and multi objective, constained aerodynamic shape optimization studies are performed. The inlet cover is placed in a FFD box and the control points in the box become the optimization variables. In single-objective optimization cases, the drag minimization or the opening moment maximization with drag constraint are considered. Additionally, a multi-objective optimization is performed to balance the conflicting objectives of drag reduction and the opening moment maximization. Through detailed analyses of optimization outcomes, including graphical representations and comparative assessments, the results of the optimization methodologies employed are presented.

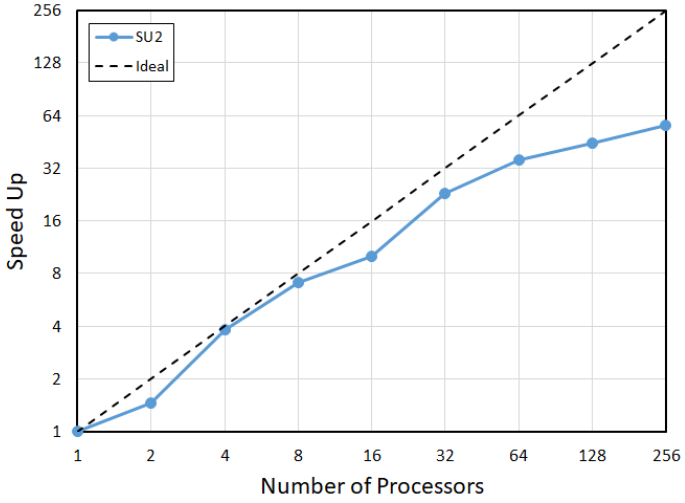

Figure 3.27: Parallel Performance of the SU2 Solver

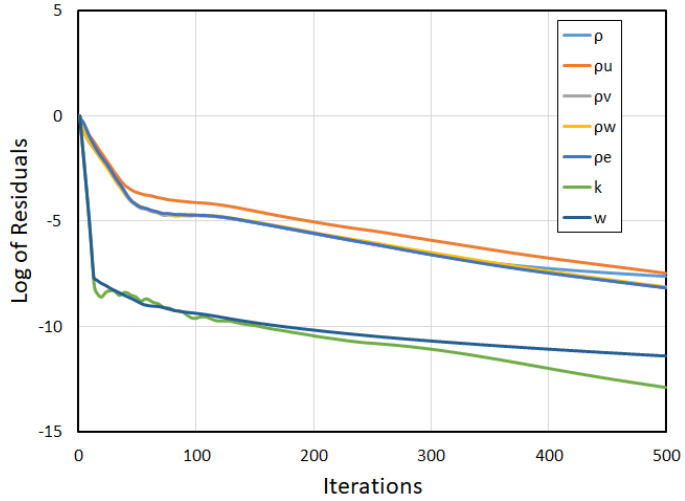

Figure 3.28: History of Residuals

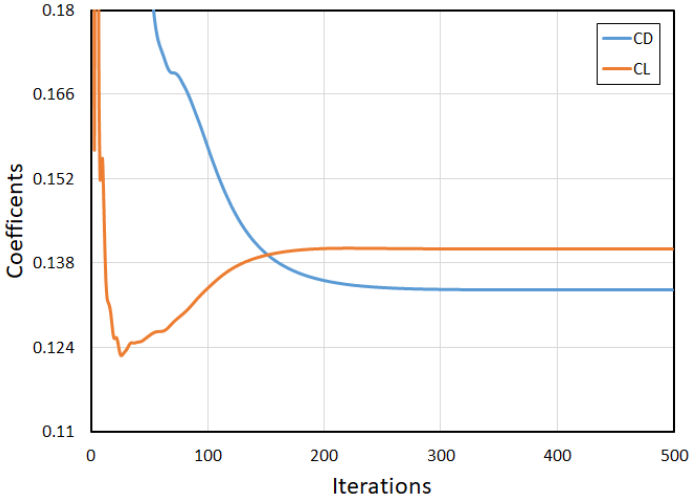

Figure 3.29: History of Aerodynamic Coefficients

3.6.1 Free Form Deformation Box and Geometric Constraints

In the optimization study, FFD boxes are employed to represent and deform the aerodynamic surfaces. An FFD box encapsulates the cover surface, as illustrated in Figure 3.30. The region inside the FFD box is defined as the design space. FFD boxes have control points along the cartesian coordinates. Since their movement deforms the surface encapsulated, the position of the FFD box control points becomes the optimization variable. Each control point is associated with three variables due to its movement in three directions in space. Visual representations of control points are given in Figure 3.31. The control points on the red planes are not allowed to move during the optimization process to keep the root section of the inlet cover fixed. In addition, the control points on the green planes are restricted to move within the plane to maintain a flat top surface. The remaining control points can move freely in three directions as long as they stay within the initial box region.

To investigate the effect of FFD box resolution in the optimization study, two FFD boxes with different numbers of control points are employed: One with a resolution of $9\times9\times9$ and the other one with a resolution of $12\times12\times12$. The FFD boxes are shown in Figure 3.32. How the FFD box resolution influences the optimum configuration is assessed in the next section.

3.6.2 Case I: Minimization of the Inlet Cover Drag

In this section, the single-objective aerodynamic shape optimization for the inlet cover is considered. The goal is to minimize the drag due to the inlet cover while meeting the geometric constraints outlined in Section 3.6.1. The objective function f is simply expressed as

$$f = \mathrm{CD}_{\mathrm{cover}} \tag{3.2}$$

The optimization process iteratively updates the design variables to achieve the improved aerodynamic performance with a lower drag coefficient. The adjoint solution provides the surface sensitivity of the baseline cover, as shown in Figure 3.33. The

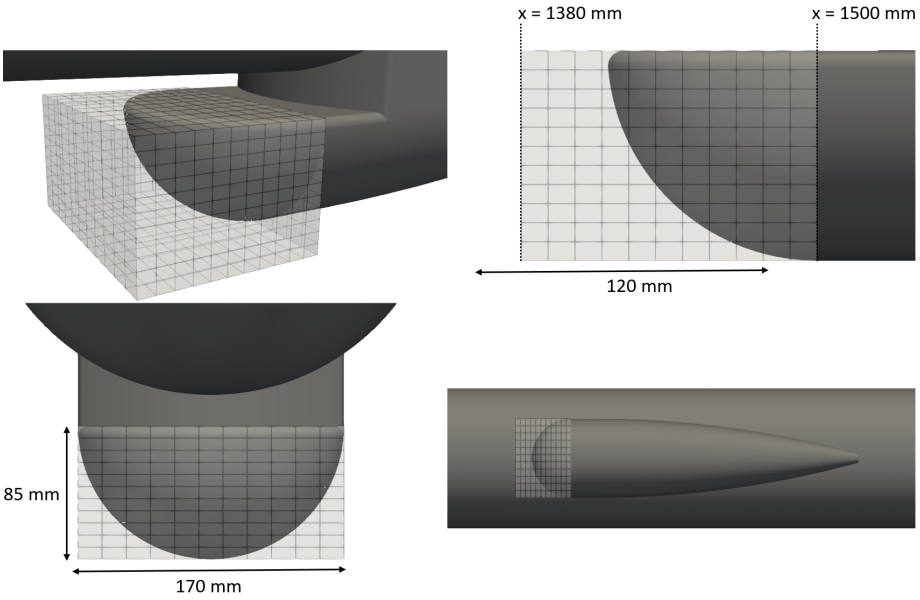

Figure 3.30: FFD Box over Inlet Cover

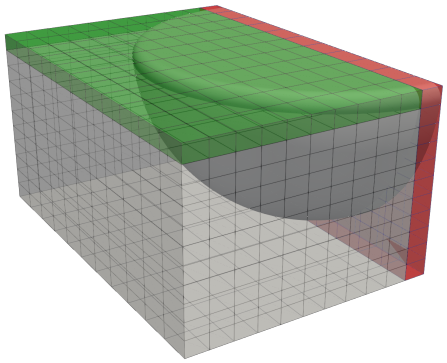

Figure 3.31: Control Points of the FFD Box

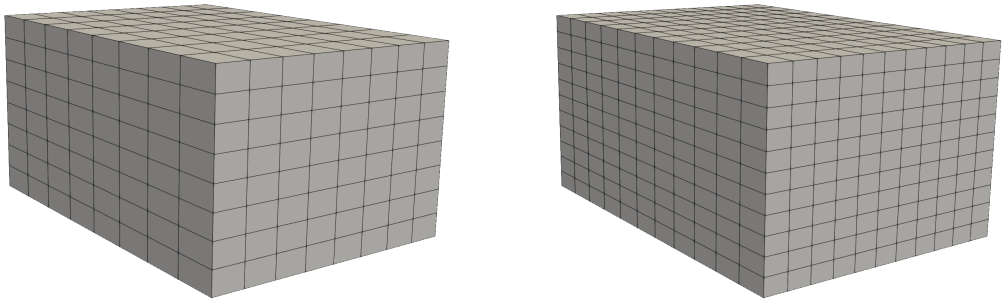

(a) Resolution of $9 \times 9 \times 9$

(b) Resolution of $12 \times 12 \times 12$

Figure 3.32: FFD Box Resolutions

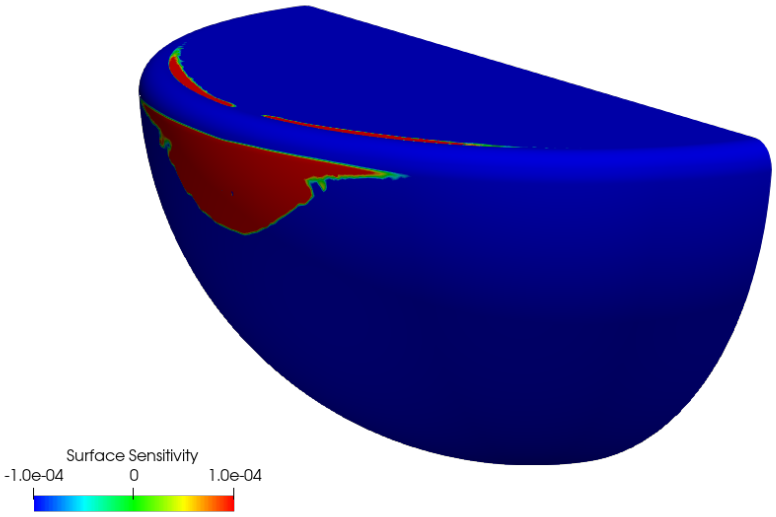

Figure 3.33: Surface Sensitivity of the Baseline Inlet Cover

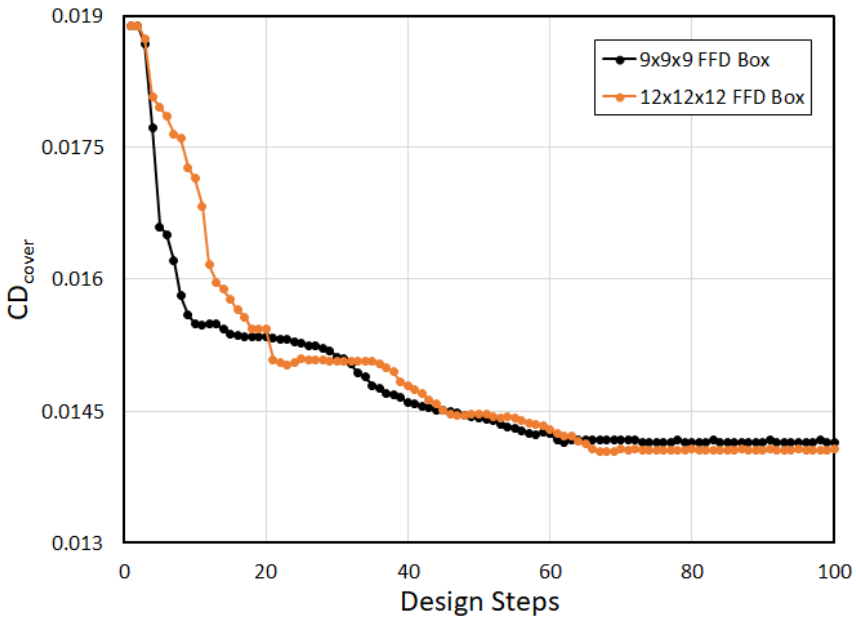

Figure 3.34: Variation of Drag Coefficient on the Inlet Cover through Optimization Steps

optimization is performed for two FFD boxes, each with a different resolution, as given in Figure 3.34. The graph traces the evolution of the drag coefficient of the inlet cover throughout the optimization processes. Both optimization processes with the $9 \times 9 \times 9$ and $12 \times 12 \times 12$ FFD boxes converge toward the same optimal design conditions. Since the large number of design variables do not cause any inefficiency in adjoint based gradient computations, the $12 \times 12 \times 12$ FFD box is chosen for conducting the optimization studies in this thesis.

The surface sensitivities in Figure 3.33 represent the change in the objective due to the perturbation of the surface nodes in the direction normal to the surface. Thus, the nodes with positive values tend to move outward, whereas those with negative values move inward to pursue the optimization objective. It can be said that while the tip of the cover tends to move out in the direction of the surface normal, there is a general tendency for inward movement on the remaining parts.

Initially, a sharp decline in the drag coefficient of the cover is observed, succeeded by a gradual decrease until the value stabilizes around design number 63. The drag coefficient of the baseline cover reduced from 0.0189 to 0.0142, signifying a 25 percent reduction.

The profiles of the optimization steps on the symmetry plane are presented in Figure 3.35. The baseline blunt quarter-sphere profile transforms into a streamlined shape through forward elongation and a thinner leading edge. Also, it is observed that the baseline design moves radially inward on the other side.

Figure 3.36 shows the inlet cover shapes obtained during the optimization steps, progressively showcasing the design evolution from a quarter-sphere to a more streamlined form by elongating forward. Additionally, the area of the top surface expands and transitions from the circular to a rectangular shape. The optimization steps after 63 are not presented since the shapes are almost identical. The comparison between the baseline and optimized designs is presented in Figure 3.37.

Figure 3.38 shows the pressure distributions for the baseline and optimum designs. The baseline configuration displays a larger region with higher pressure values at the tip of the cover compared to the optimum design. In both designs, the low-pressure

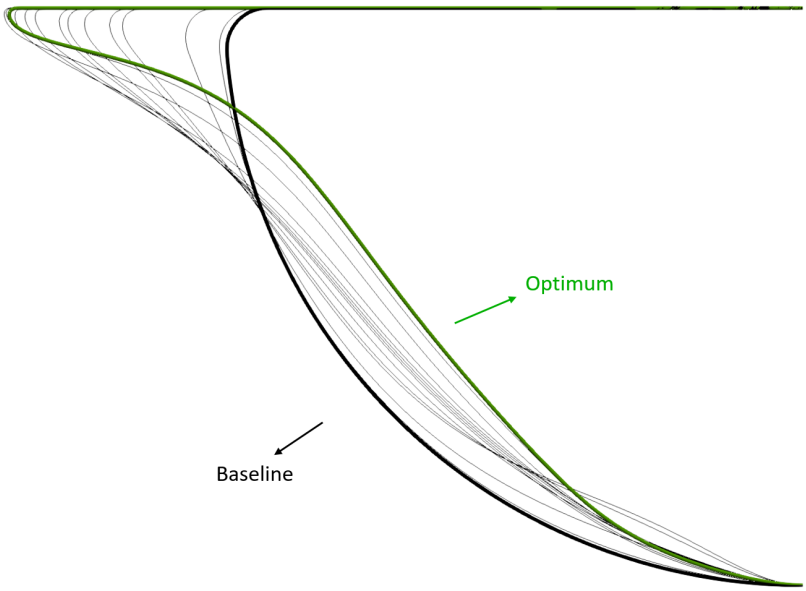

Figure 3.35: Inlet Cover Profiles through Optimization Steps

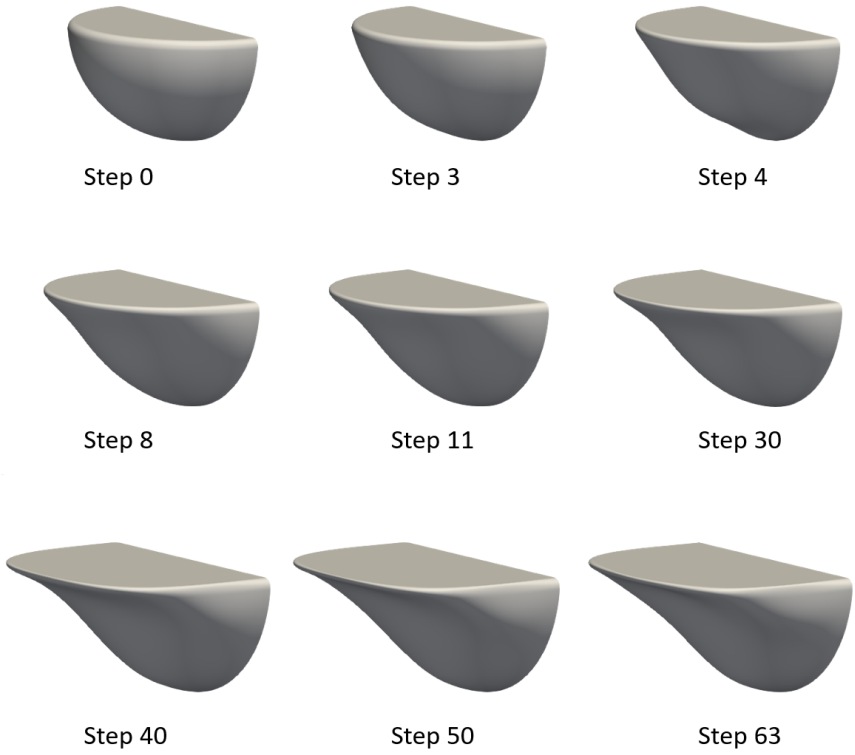

Figure 3.36: Inlet Cover Shapes through Optimization Steps

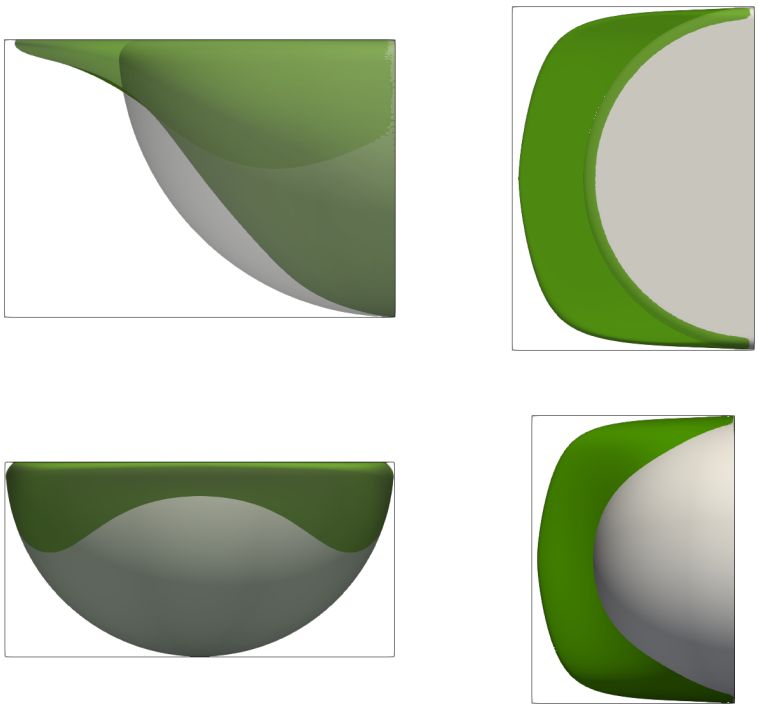

Figure 3.37: Baseline and Optimum Inlet Cover Shapes

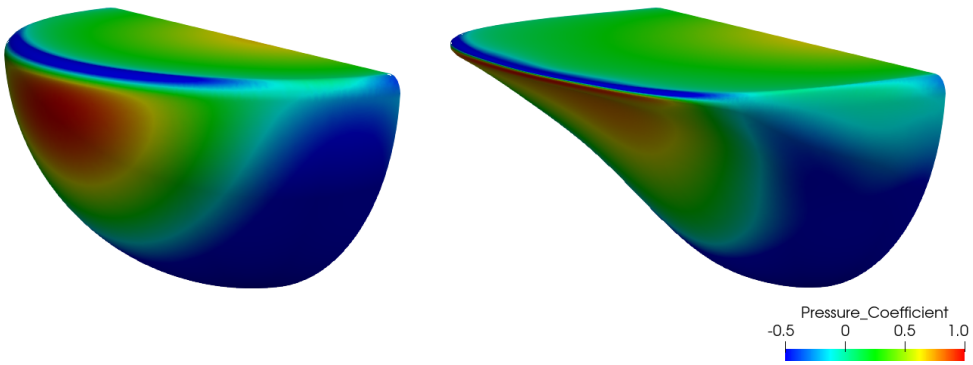

Figure 3.38: Surface Pressure Distribution on Baseline (left) and Optimum (right) Inlet Covers

regions are observed on the sides and bottom where the inlet cover widens. These areas are also called suction regions and have a decreasing effect on drag.

The pressure distributions for the baseline and optimum designs on the symmetry plane are illustrated in Figure 3.39. The high-pressure region at the tip of the baseline cover is less prominent in the optimum design. Furthermore, a low-pressure area is evident at the bottom end of the cover in both designs.

The Mach number distributions for the baseline and optimum designs on the symmetry plane are depicted in Figure 3.40. The baseline design features a stagnation point near the tip of the cover, while the optimum design has a significantly reduced stagnation region with an almost absent stagnation point. The flow below the stagnation point accelerates in both designs. Also, a pocket of high-speed flow region exists at the beginning of the top surface of the covers.

To examine whether changing the cover shape affects the other components, Figure 3.41 illustrates the drag components of baseline and optimum configurations. As anticipated, the most significant change is observed in the cover due to the deformation taking place for this component. It results in a 25% reduction in the inlet cover drag. It is also evident that the change in the cover shape influences the shell component, which is adjacent to the cover. The 6% reduction in the drag of the shell is observed. The drag of the other components remains relatively unchanged.

Table 3.8: Aerodynamic Loads for Case I

	CM_{cover}	CD_{cover}	C_D
Baseline	-0.0032	0.0189	0.1335
Optimum	-0.0162	0.0142	0.1276

The aerodynamic loads for the baseline and the optimum configurations are presented in Table 3.8. The drag coefficient of the cover has been reduced from 0.0189 to 0.0142, indicating a 25% reduction. Additionally, the overall configuration's drag coefficient decreases from 0.1335 to 0.1276, reflecting a 4% reduction. Meanwhile, the moment coefficient of the cover with respect to the hinge axis changes from -0.0032 to -0.0162. The negative sign of the moment coefficient indicates a moment in the

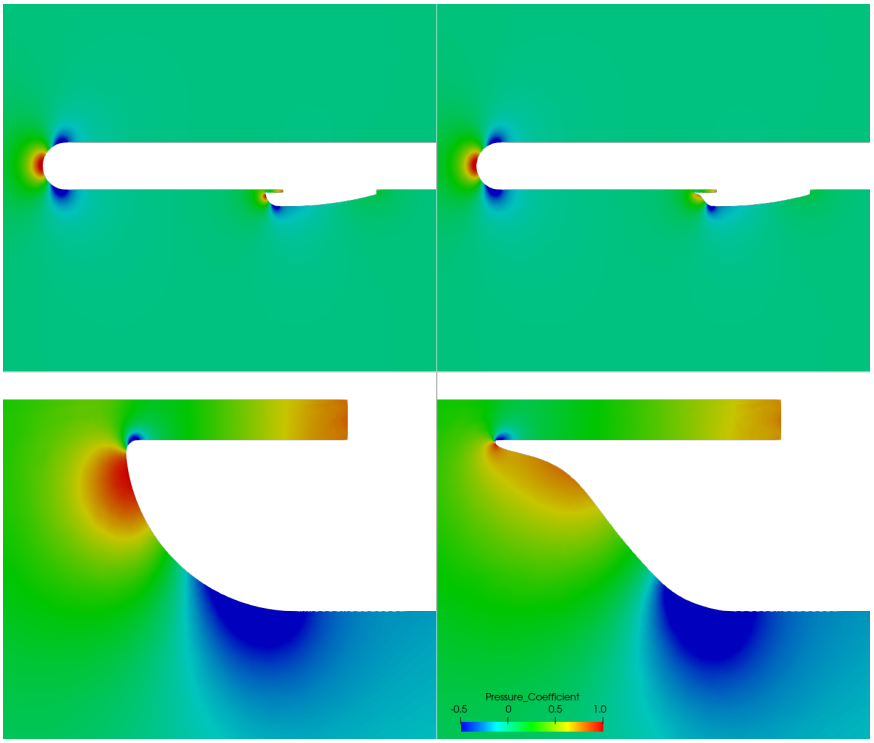

Figure 3.39: Pressure Distribution on Symmetry Plane for Baseline (left) and Optimum (right) Configurations

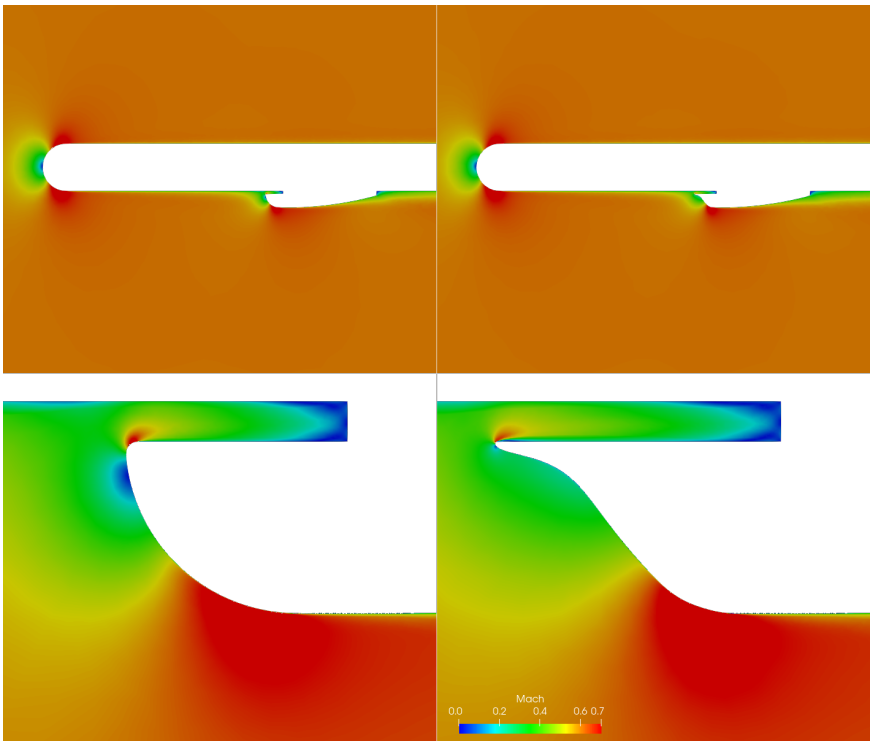

Figure 3.40: Mach Number Distribution on Symmetry Plane for Baseline (left) and Optimum (right) Configurations

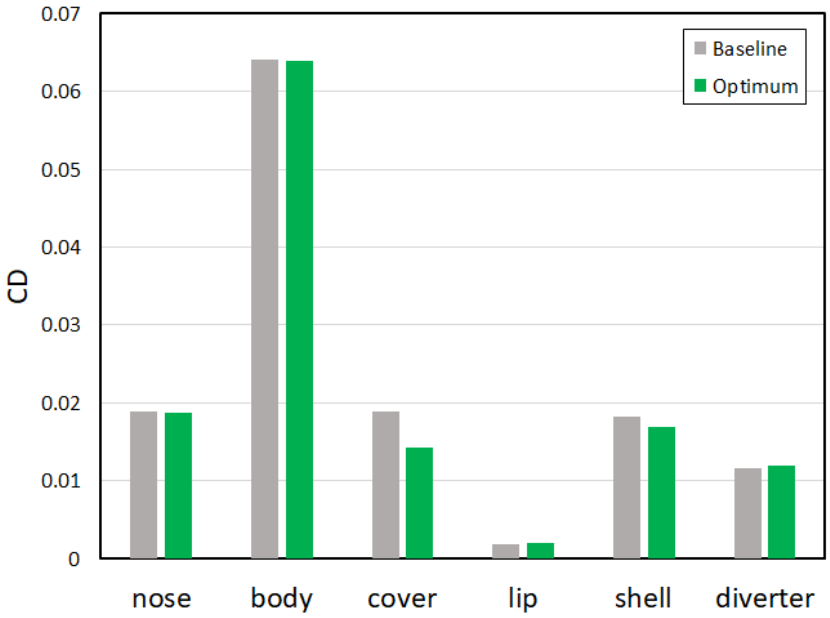

Figure 3.41: Component Drag Coefficients

closing direction. A lower value implies a greater moment in the closing direction for the cover, which is undesirable.

3.6.3 Case II: Constrained Maximization of the Inlet Cover Opening Moment

This section focuses on another single-objective aerodynamic shape optimization of the inlet cover. The aim is to maximize the opening moment of the cover with respect to the hinge axis, starting from the same baseline geometry. The location of the hinge axis is shown in Figure 3.42.

In this case, alongside the geometric constraints outlined in Section 3.6.1, the drag coefficient of the overall configuration is also incorporated as a constraint. The reason is to prevent a dramatic increase in drag and to avoid the generation of unfeasible inlet cover shapes. Therefore, C_D is constrained, and it has an upper limit of 0.146, which is 10 percent higher than the baseline value. The objective function f and constraint function g can be expressed as

$$f = \mathrm{CM}_{\mathrm{cover}} \tag{3.3}$$

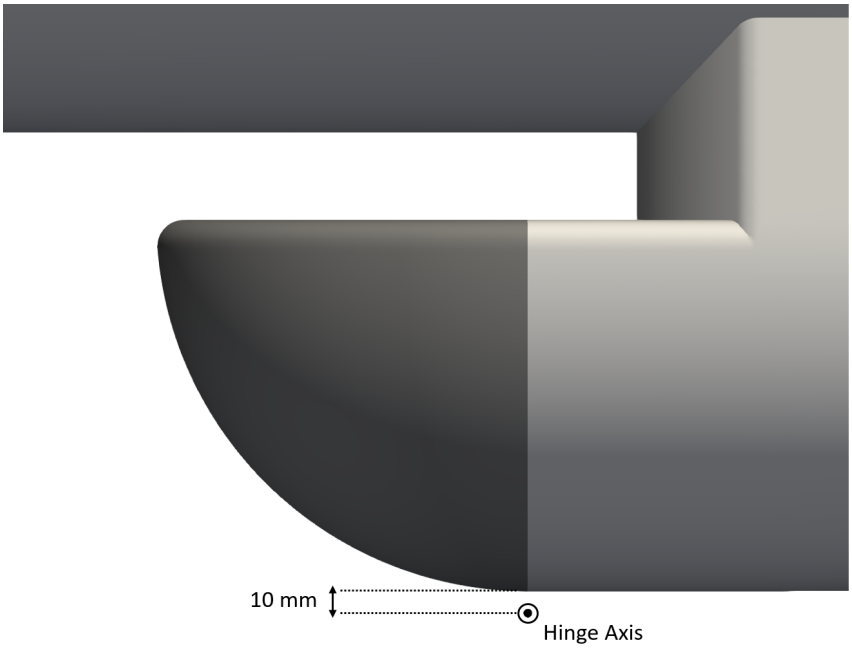

Figure 3.42: Inlet Cover Hinge Axis

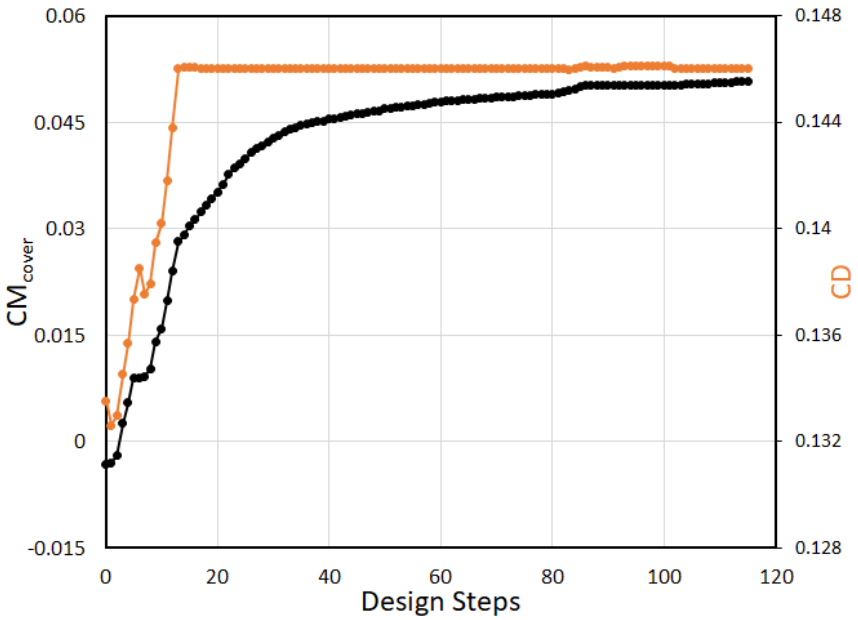

Figure 3.43: Variation of CM_{cover} and C_D through Optimization Steps

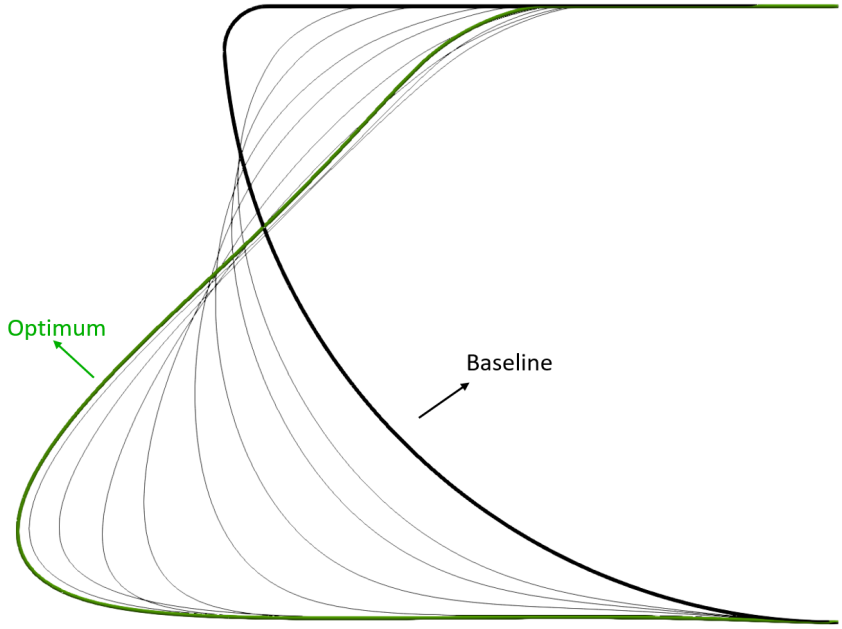

Figure 3.44: Variation of Inlet Cover Profiles through Optimization Steps

$$g = \text{CD} < 1.1 \times \text{CD}_{\text{baseline}} \tag{3.4}$$

Figure 3.43 presents the optimization history, illustrating CM_{cover} and C_D against the optimization steps. This graph tracks the moment coefficient of the cover with respect to the hinge axis and the drag coefficient of the overall configuration throughout the optimization process. Initially, there is an abrupt increase in the CM_{cover} and C_D. By the optimization step 13, the drag coefficient of the overall configuration reaches 0.146, which serves as the upper limit of the drag constraint. However, CM_{cover} continues to rise gradually while C_D stays constant. The moment coefficient converges around the step 90. By the conclusion of the optimization process, the moment coefficient of the cover relative to the hinge axis increases from -0.0032 to 0.0399.

The profiles of the optimization steps on the symmetry plane are illustrated in Figure 3.44. Throughout the optimization process, the tip of the cover gradually shifts from being adjacent to the top surface to becoming adjacent to the bottom surface, while its leading edge becomes more blunt. Additionally, the cover elongates forward, and

the area of the top surface shrinks.

The inlet cover shapes obtained during the optimization steps are illustrated in Figure 3.45. The gradual rounding of the shape up to design 8 is followed by a downward tapering and formation of an inclined plane on the front surface. The shapes after the step 90 are not presented since the shapes are almost identical. The comparison between the baseline and optimum configurations is presented in Figure 3.46.

The pressure distributions for the baseline and optimum designs are shown in Figure 3.47. As observed the high-pressure area on the inclined plane generates an opening moment on the hinge axis. Additionally, a mild pressure drop is observed in the transition region between the inclined plane and the top surface of the inlet cover.

The pressure distributions on the symmetry plane for the baseline and optimum designs are illustrated in Figure 3.48. In the optimum design, the area of the high-pressure region enlarges. Furthermore, the low-pressure region at the bottom part of the baseline cover shifts to the vicinity of the tip in the optimum design.

The Mach number distribution on the symmetry plane for the baseline and optimum designs are illustrated in Figure 3.49. In the optimum design, the pocket of the high Mach region at the beginning of the top surface enlarges. Additionally, the stagnation region moves with the tip of the cover.

The results for Case II are summarized in Table 3.9. The drag coefficient of the cover increased from 0.0189 to 0.0399. Moreover, the overall missile drag coefficient climbed from 0.1335 to 0.146, reaching the constraint's upper limit. The moment coefficient of the cover, relative to the hinge axis, shifted from -0.0032 to 0.0359. This rise in the optimum design suggests an enhanced opening moment for the cover.

Table 3.9: Aerodynamic Loads for Case II

	CM_{cover}	CD_{cover}	C_D
Baseline	-0.0032	0.0189	0.1335
Optimum	0.0359	0.0399	0.1461

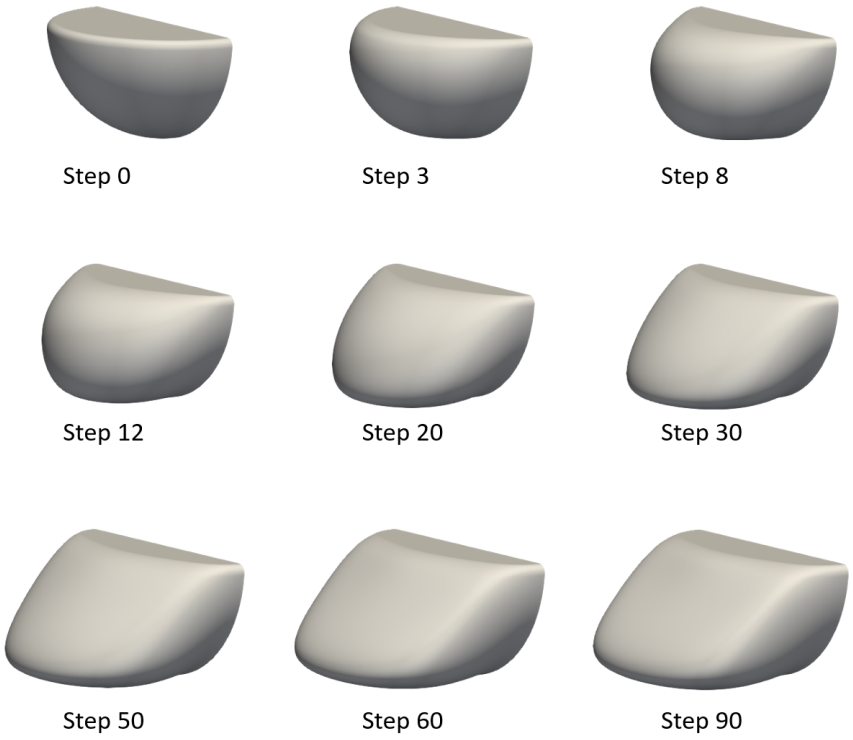

Figure 3.45: Variation of Inlet Cover Shapes through Optimization Steps

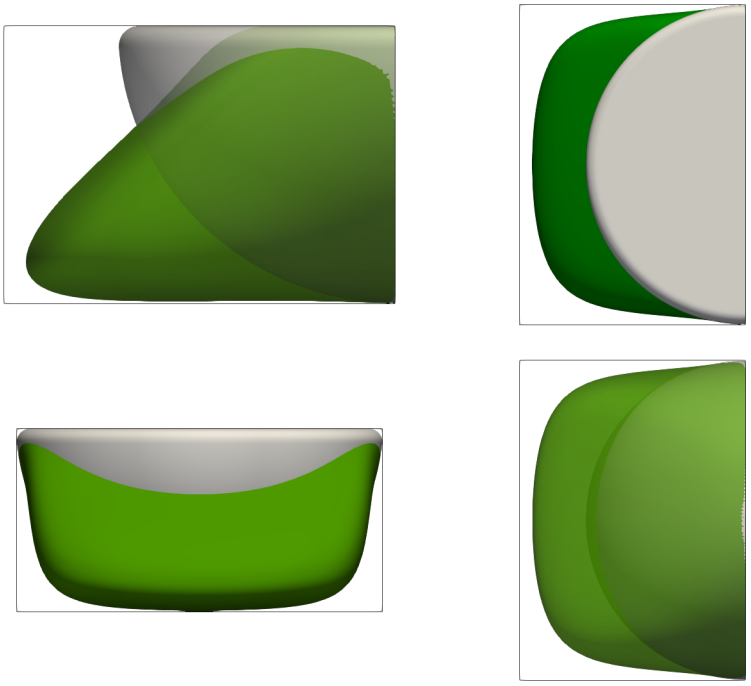

Figure 3.46: Baseline and Optimum Inlet Cover Shapes

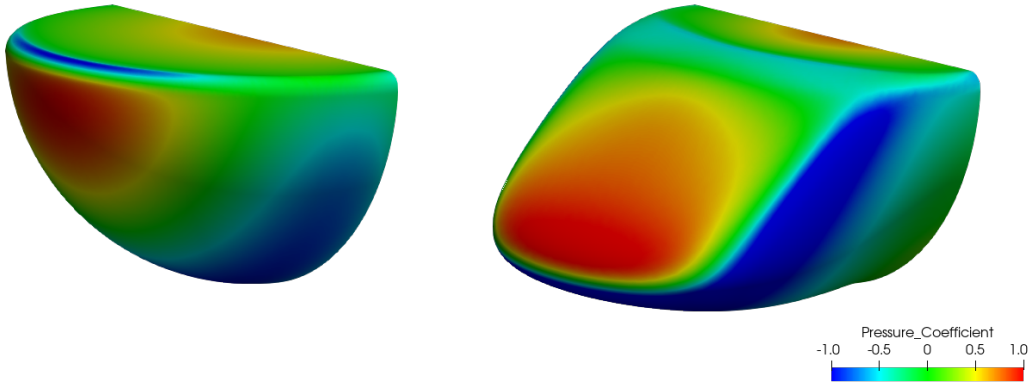

Figure 3.47: Surface Pressure Distribution on Baseline (left) and Optimum (right) Inlet Cover

3.6.4 Case III: Multi-objective Optimization

Next, a multi-objective optimization is performed in the pursuit of improving the aerodynamic performance of the inlet cover. The main objective is to reach an optimal balance between the conflicting objectives, namely, to minimize the drag due to the inlet cover while simultaneously increasing the opening moment with respect to the hinge axis. To effectively implement this objective, a weighting factor is introduced into the objective function:

$$f(c) = \mathrm{CD}_{\mathrm{cover}} - c \times \mathrm{CM}_{\mathrm{cover}} \tag{3.5}$$

This approach facilitates the incorporation of multiple performance criteria simultaneously and provides a more nuanced understanding of aerodynamic shape optimization for the inlet cover. In the optimization process, minimizing the function f is the main objective. Optimization can take place for any value of c. As the c increases, the importance of $\mathrm{CM}_{\mathrm{cover}}$ is amplified while decreasing c reduces its weight. When c equals zero, it represents the single objective drag minimization problem.

Figure 3.50 depicts a Pareto front, showcasing how changes in the weighting factor c impact the relationship between $\mathrm{CD}_{\mathrm{cover}}$ and $\mathrm{CM}_{\mathrm{cover}}$ as part of the optimization process, where the objective is minimizing the objective function f. It also presents baseline values alongside optimization outcomes from Case I and Case II. This com-

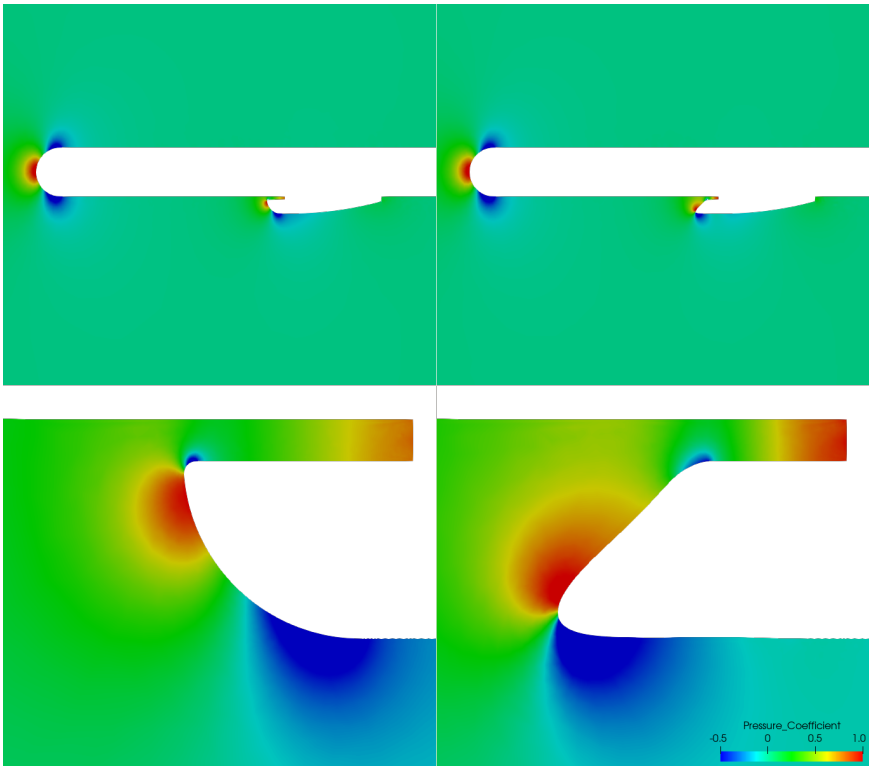

Figure 3.48: Pressure Distribution on Symmetry Plane for Baseline (left) and Optimum (right)

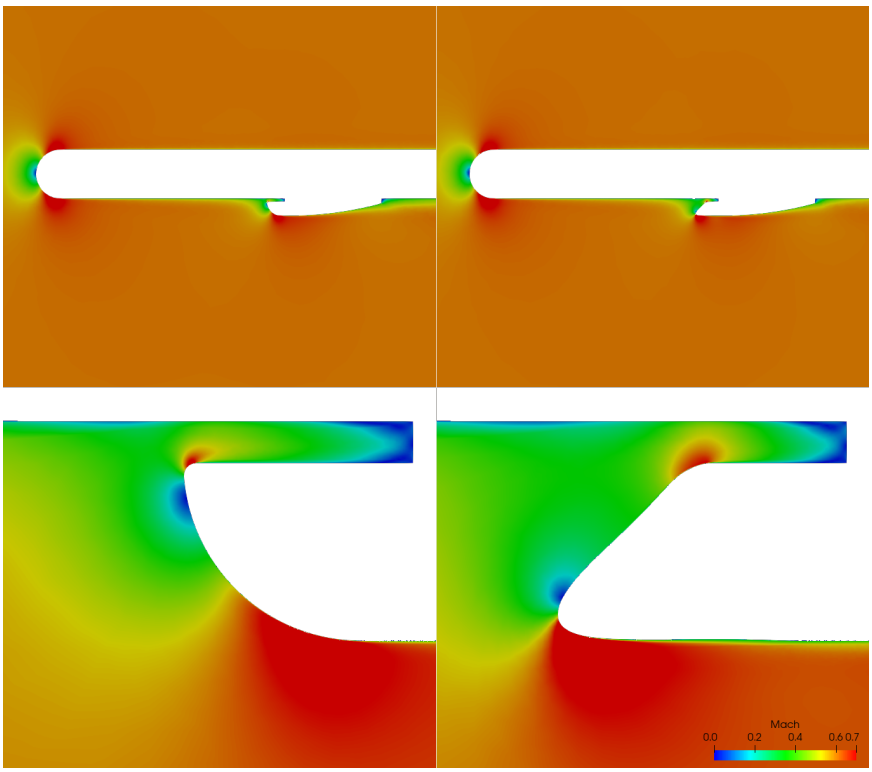

Figure 3.49: Mach Number Distribution on Symmetry Plane for Baseline (left) and Optimum (right)

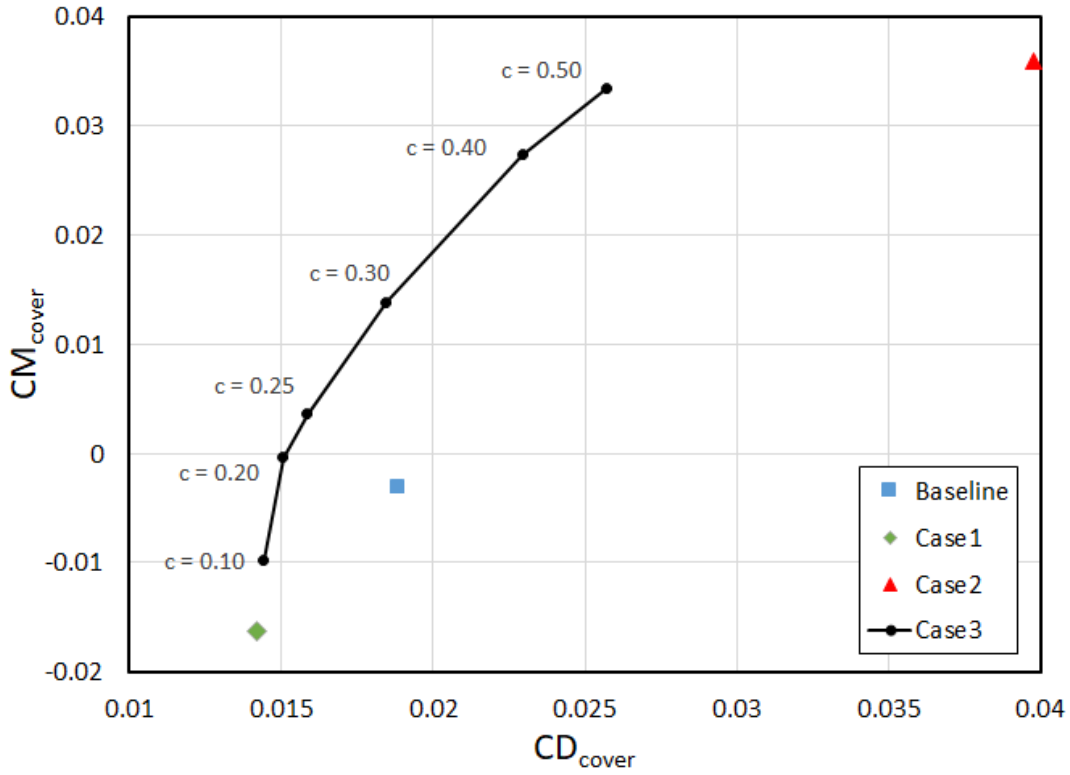

Figure 3.50: Pareto Front for Optimum Designs

parison offers a comprehensive understanding of the improvements achieved through the optimization process across different objectives. This graphical representation offers a clear insight into how adjusting c influences the trade-off between drag reduction and pitching moment control during the optimization process.

As the value of c increases, both the opening moment and drag of the cover increase. However, all values of Case III fall between Case I and Case II, providing alternative choices compared to the baseline. For $c = 0.1$, the drag is slightly higher than in Case I, yet the CM_{cover} increases. Moving to $c = 0.2$, the drag decreases compared to the baseline, and the CM_{cover} is around zero. At $c = 0.25$, there's a rise in drag compared to $c = 0.2$, but it comes with a positive opening moment. Progressing to $c = 0.3$, despite the drag being similar to the baseline, an increased opening moment is observed. Finally, for $c = 0.4$ and $c = 0.5$, although the drag increases sharply, they offer high values of the opening moment, with significantly lower drag compared to Case II.

The inlet cover shapes corresponding to each value of c are illustrated in Figures 3.51.

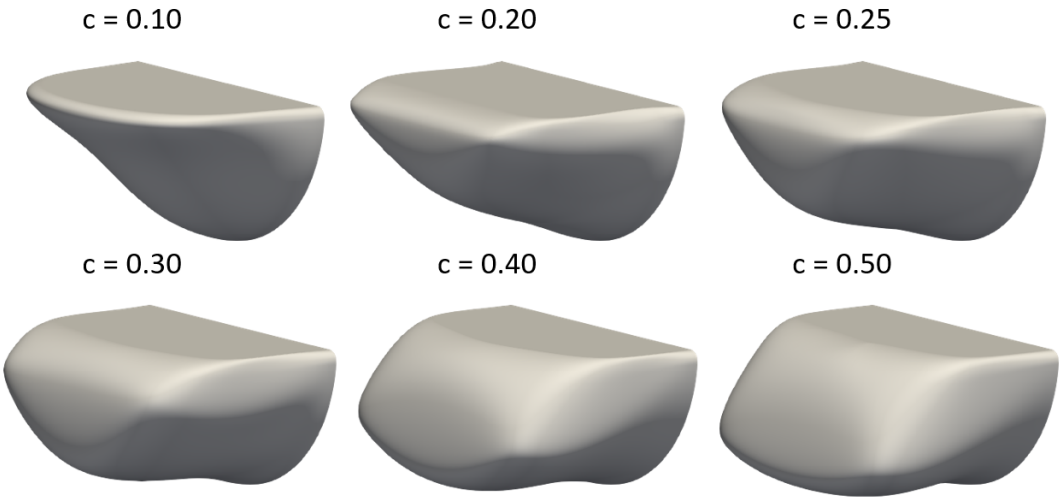

Figure 3.51: Inlet Cover Shapes for Optimum Designs

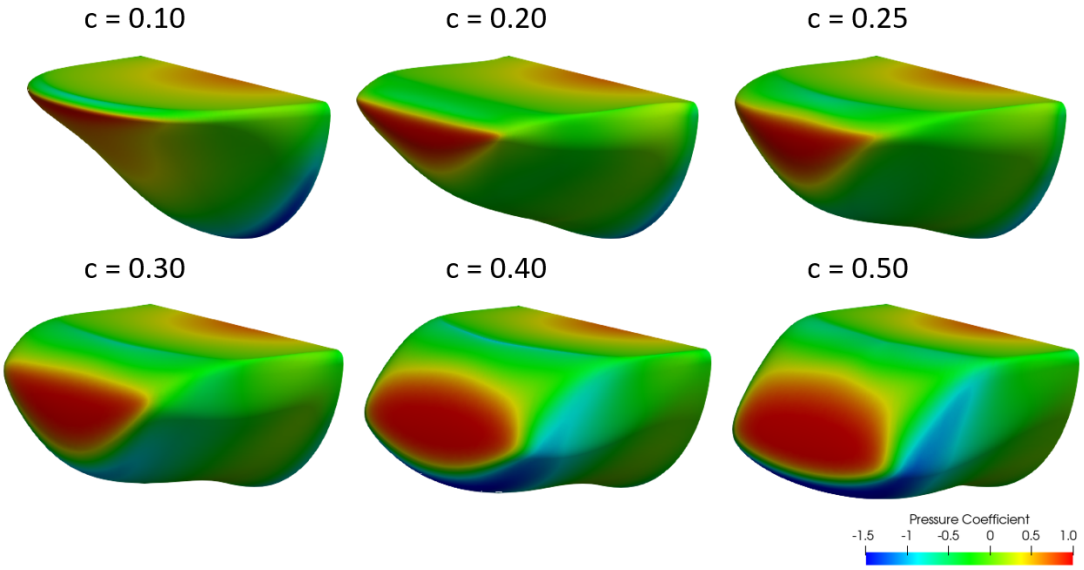

Figure 3.52: Surface Pressure Distribution on Optimum Designs

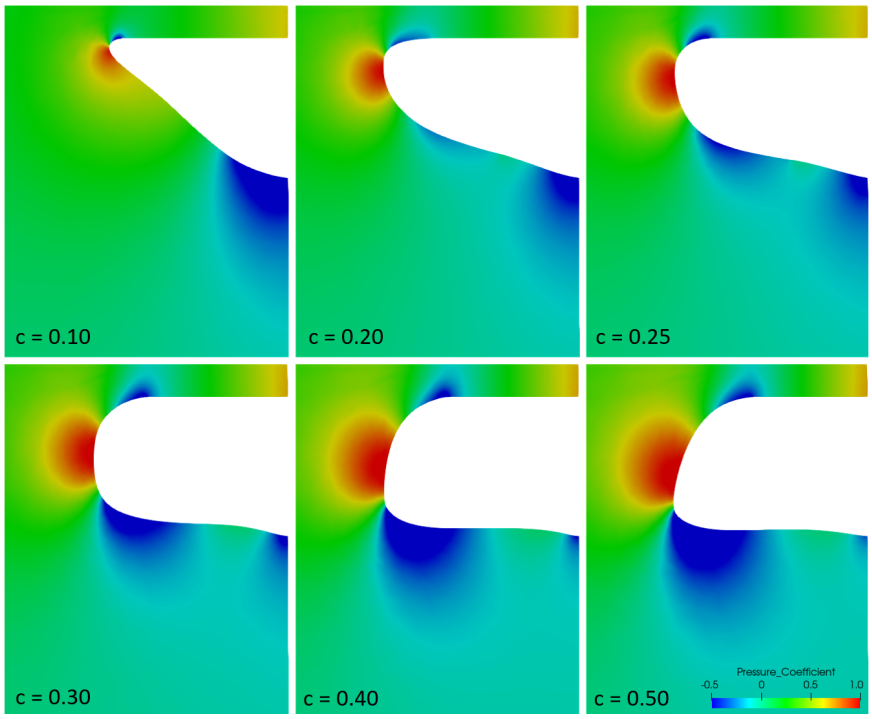

Figure 3.53: Pressure Distribution on Symmetry Plane for Optimum Designs

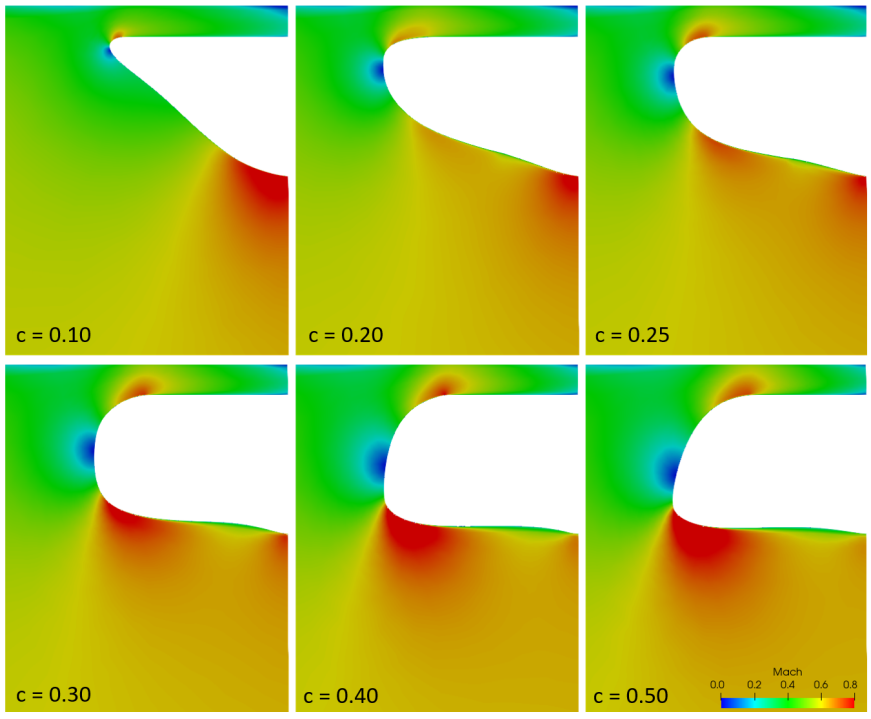

Figure 3.54: Mach Number Distribution on Symmetry Plane for Optimum Designs

It's observed that as the value of c increases, the cover shape loses its streamlined form. Specifically, the shape of $c = 0.1$ resembles Case 1, while $c = 0.5$ resembles Case 2. As c increases, the sharpness at the tip of the top surfaces disappears, and the inclined front surface becomes more pronounced. From $c = 0.2$ to $c = 0.5$, there's a decrease in the length of the optimal designs, accompanied by a reduction in the top surface area.

The pressure distributions corresponding to each value of c are illustrated in Figures 3.52. As c increases, several observations emerge. The high-pressure region on the front surface enlarges, while a low-pressure region between the front and bottom surfaces becomes obvious. Additionally, the pressure distribution on the top flat surface remains relatively similar across different values of c.

The pressure distributions on the symmetry plane for each value of c are depicted in Figure 3.53. As c increases, the high-pressure region enlarges. Additionally, the low-pressure region at the right side of the bottom surface, where the cover and shell meet, becomes less observable. Conversely, a new low-pressure area emerges at the left side of the bottom surface of the cover. Finally, a low-pressure region at the beginning of the top surface becomes more noticeable.

The Mach number distributions for each value of the factor c are illustrated on the symmetry plane in Figure 3.54. As c increases, several trends become apparent. Firstly, the high Mach number region at the root of the cover, where the cover and shell meet, diminishes. Additionally, the stagnation region becomes more distinct. Furthermore, a new high Mach number area emerges at the left side of the bottom surface of the cover. Lastly, the high Mach number pocket at the left of the top surface enlarges.

The aerodynamic performances of the inlet cover for both the baseline and optimum designs from all three cases are given in Table 3.10.

Table 3.10: Aerodynamic Loads for the Optimum Designs

	CM_{cover}	CD_{cover}	C_D
Baseline	-0.0032	0.0189	0.1335
Case I	-0.0162	0.0142	0.1276
Case II	0.0359	0.0399	0.1460
Case III (c = 0.50)	0.0334	0.0257	0.1385
Case III (c = 0.40)	0.0273	0.0230	0.1364
Case III (c = 0.30)	0.0138	0.0185	0.1329
Case III (c = 0.25)	0.0036	0.0159	0.1306
Case III (c = 0.20)	-0.0004	0.0151	0.1300
Case III (c = 0.10)	-0.0098	0.0144	0.1290

CHAPTER 4

CONCLUSIONS

In this thesis, an adjoint-based aerodynamic shape optimization of a missile engine inlet cover is successfully performed. The SU2 flow and adjoint solvers are utilized to minimize the drag and to maximize the opening moment of an engine inlet cover to enhance the capabilities of the missile system. The baseline missile configuration is inspired by the ÇAKIR cruise missile. Suitable design conditions are selected as a Mach number of 0.6 and an altitude of 5000 m.

The Open-source SU2 CFD suit is first verified to predict the flow fields over missile configuration accurately. The Hemisphere Cylinder and NASA TM X-3070 missile test cases are studied. The Hemisphere Cylinder verification study shows that the SU2 solver accurately predicts the pressure distributions along the spherical shapes. Both the SA and SST turbulence models yield consistent flow predictions and agree well with the experimental data. The choice of turbulence model has a negligible impact on the aerodynamic load coefficients. Similarly, the NASA TM X-3070 missile study reveals that the aerodynamic load coefficients are computed accurately with the choice of proper grid densities, and they are in agreement with the experimental data. The grid independence study is conducted for the baseline configuration, and it provides a balance between the accuracy and the computational cost. The computations are performed in parallel, and the high parallel efficiency of the SU2 solver is assessed.

The Optimization studies focus on three distinct cases, each targeting different objectives. In Case I, the drag due to the engine inlet cover is minimized, whereas in Case II the opening moment of the inlet cover is maximized with a constraint on the drag. In Case III, a weighted, two-objective optimization is performed, and a Pareto front

for the minimum drag and the maximum opening moment is obtained.

In Case I, a single-objective optimization is performed to minimize the drag due to the engine inlet cover. This optimization process yields a noticeable change in the cover's shape and a 25% reduction in the drag compared to the baseline configuration.

In Case II, the objective is shifted to maximize the opening moment of the inlet cover with respect to the hinge axis, while the drag rise is constrained by a maximum 10% increase. The optimization process successfully increases the opening moment while the total drag reaches the upper bound. The initial opening moment of the baseline cover, with a negative moment coefficient of -0.0032, transitions to a closing moment, which is the moment to be applied to keep the inlet cover closed, with a significant increase in magnitude, 0.0359.

In Case III, a multi-objective optimization is undertaken by introducing a weighting factor to balance the competing objectives of drag reduction and opening moment enhancement. The variation of the weighting factor produces a Pareto front of the competing objectives, which facilitates the discovery of optimal designs capable of simultaneously reducing drag and enhancing the opening moment. For instance, $c = 0.20$ case provides the minimum opening moment with $\text{CM}_{\text{cover}} = -0.0004$ while the drag induced is still less than the baseline drag, $\text{CD}_{\text{cover}} = 0.0151$. For $c = 0.30$, the drag induced is the same as the baseline configuration, but the inlet cover opens by itself once it is released. The Pareto front gives the designer a set of configurations to choose from based on the opening moment specifications and the required drag minimization.

The study shows that with CFD simulations and the adjoint-based shape optimization approach, significant improvements in the aerodynamic performance of the inlet cover are achieved, and an optimum design can be reached against the conflicting and competing objectives. In addition, the present findings strongly indicate that the design of the missiles, where aerodynamic performance plays a critical role, can be significantly enhanced by adjoint-based shape optimization studies.

REFERENCES

[1] "Tomahawk subsonic cruise missile." https://airandspace.si.edu/collection-objects/missile-cruise-ship-launched-tomahawk-bgm-109/nasm_A19820119000.

[2] K. Parise, "Functional ground testing - evaluating the tomahawk cruise missile," in *30th Aerospace Sciences Meeting and Exhibit*, 1992.

[3] K. C. Giannakoglou and D. I. Papadimitriou, *Adjoint Methods for Shape Optimization*, pp. 79–108. Berlin, Heidelberg: Springer Berlin Heidelberg, 2008.

[4] J. H. Anthony and J. W. William, "Air intake cover."

[5] G. Von Groll and D. J. Ewins, "On the dynamics of windmilling in aero-engines," in *IMechE Conference Transactions*, vol. 6, pp. 721–730, Citeseer, 2000.

[6] S. P. Grossman and S. K. Laird, "Airstream ejected missile engine inlet cover," Aug. 26 1997. US Patent 5,660,357.

[7] S. N. Skinner and H. Zare-Behtash, "State-of-the-art in aerodynamic shape optimisation methods," *Applied Soft Computing*, vol. 62, pp. 933–962, 2018.

[8] Y. Nesterov and V. Spokoiny, "Random gradient-free minimization of convex functions," *Foundations of Computational Mathematics*, vol. 17, no. 2, pp. 527–566, 2017.

[9] P. Gage and I. Kroo, "A role for genetic algorithms in a preliminary design environment," *Aircraft Design, Systems, and Operations Meeting*, Aug 1993.

[10] M. B. Anderson, J. E. Burkhalter, and R. M. Jenkins, "Missile aerodynamic shape optimization using genetic algorithms," *Journal of Spacecraft and Rockets*, vol. 37, p. 663–669, Sep 2000.

[11] K. Yamamoto and O. Inoue, "Applications of genetic algorithm to aerodynamic shape optimization," *12th Computational Fluid Dynamics Conference*, Jun 1995.

[12] T. L. Holst, "Genetic algorithms applied to multi-objective aerodynamic shape optimization," tech. rep., 2005.

[13] J. R. Martins and A. Ning, *Engineering design optimization*. Cambridge University Press, 2021.

[14] W. K. Anderson and V. Venkatakrishnan, "Aerodynamic design optimization on unstructured grids with a continuous adjoint formulation," *Computers & Fluids*, vol. 28, no. 4-5, pp. 443–480, 1999.

[15] A. Bryson and Y. Ho, *Applied Optimal Control: Optimization, Estimation, and Control*. Blaisdell book in the pure and applied sciences, Blaisdell Publishing Company, 1969.

[16] J. Arora and E. Haug Jr, "Efficient optimal design of structures by generalized steepest descent programming," *International Journal for Numerical Methods in Engineering*, vol. 10, no. 4, pp. 747–766, 1976.

[17] O. Pironneau, "On optimum profiles in stokes flow," *Journal of Fluid Mechanics*, vol. 59, no. 1, pp. 117–128, 1973.

[18] A. Jameson, "Aerodynamic design via control theory," *Journal of scientific computing*, vol. 3, pp. 233–260, 1988.

[19] A. Jameson, L. Martinelli, and N. A. Pierce, "Optimum aerodynamic design using the navier–stokes equations," *Theoretical and computational fluid dynamics*, vol. 10, no. 1, pp. 213–237, 1998.

[20] M. Schramm, B. Stoevesandt, and J. Peinke, "Optimization of airfoils using the adjoint approach and the influence of adjoint turbulent viscosity," *Computation*, vol. 6, no. 1, p. 5, 2018.

[21] S. T. LeDoux, J. C. Vassberg, D. P. Young, S. Fugal, D. Kamenetskiy, W. P. Huffman, R. G. Melvin, and M. F. Smith, "Study based on the aiaa aerodynamic

design optimization discussion group test cases," *AIAA Journal*, vol. 53, no. 7, pp. 1910–1935, 2015.

[22] S. Chen, Z. Lyu, G. K. Kenway, and J. R. Martins, "Aerodynamic shape optimization of common research model wing–body–tail configuration," *Journal of Aircraft*, vol. 53, no. 1, pp. 276–293, 2016.

[23] C. Ma, X. Su, and X. Yuan, "An efficient unsteady adjoint optimization system for multistage turbomachinery," *Journal of Turbomachinery*, vol. 139, no. 1, p. 011003, 2017.

[24] T. Dhert, T. Ashuri, and J. R. Martins, "Aerodynamic shape optimization of wind turbine blades using a reynolds-averaged navier–stokes model and an adjoint method," *Wind Energy*, vol. 20, no. 5, pp. 909–926, 2017.

[25] C. Othmer, "Adjoint methods for car aerodynamics," *Journal of Mathematics in Industry*, vol. 4, no. 1, p. 6, 2014.

[26] J. Deng, K. Zhao, L. Zhou, W. Zhang, B. Shu, J. Huang, and Z. Gao, "Aerodynamic/stealth design of s-duct inlet based on discrete adjoint method," *Applied Mathematics and Mechanics*, vol. 45, no. 4, pp. 725–746, 2024.

[27] M. Colonno, F. Palacios, T. D. Economon, A. K. Lonkar, and J. J. Alonso, "An adjoint-based aerodynamic shape optimization methodology for fairing systems," in *31st AIAA Applied Aerodynamics Conference*, p. 2649, 2013.

[28] G. Carrier, D. Destarac, A. Dumont, M. Meheut, I. Salah El Din, J. Peter, S. Ben Khelil, J. Brezillon, and M. Pestana, "Gradient-based aerodynamic optimization with the elsa software," in *52nd Aerospace Sciences Meeting*, p. 0568, 2014.

[29] G. K. Kenway, C. A. Mader, P. He, and J. R. Martins, "Effective adjoint approaches for computational fluid dynamics," *Progress in Aerospace Sciences*, vol. 110, p. 100542, Oct 2019.

[30] S. Nadarajah and A. Jameson, "A comparison of the continuous and discrete adjoint approach to automatic aerodynamic optimization," in *38th Aerospace sciences meeting and exhibit*, p. 667, 2000.

[31] J. Elliott and J. Peraire, "Practical three-dimensional aerodynamic design and optimization using unstructured meshes," *AIAA journal*, vol. 35, no. 9, pp. 1479–1485, 1997.

[32] J. E. Peter and R. P. Dwight, "Numerical sensitivity analysis for aerodynamic optimization: A survey of approaches," *Computers & Fluids*, vol. 39, no. 3, pp. 373–391, 2010.

[33] C. Elliott, "The simple essence of automatic differentiation," *Proceedings of the ACM on Programming Languages*, vol. 2, no. ICFP, pp. 1–29, 2018.

[34] D. A. Masters, D. J. Poole, N. J. Taylor, T. Rendall, and C. B. Allen, "Impact of shape parameterisation on aerodynamic optimisation of benchmark problem," in *54th AIAA Aerospace Sciences Meeting*, p. 1544, 2016.

[35] F. Palacios, T. D. Economon, A. Aranake, S. R. Copeland, A. K. Lonkar, T. W. Lukaczyk, D. E. Manosalvas, K. R. Naik, S. Padron, B. Tracey, and et al., "Stanford university unstructured (su2): Analysis and design technology for turbulent flows," *52nd Aerospace Sciences Meeting*, Jan 2014.

[36] D. C. Wilcox, *Turbulence modeling for CFD*. DCW Industries, 2010.

[37] P. SPALART and S. ALLMARAS, "A one-equation turbulence model for aerodynamic flows," *30th Aerospace Sciences Meeting and Exhibit*, Jan 1992.

[38] F. R. Menter, "Two-equation eddy-viscosity turbulence models for engineering applications," *AIAA Journal*, vol. 32, p. 1598–1605, Aug 1994.

[39] Z. Lyu, G. K. Kenway, and J. R. R. A. Martins, "Aerodynamic shape optimization investigations of the common research model wing benchmark," *AIAA Journal*, vol. 53, pp. 968–985, 2015.

[40] Z. Lyu and J. R. R. A. Martins, "Aerodynamic design optimization studies of a blended-wing-body aircraft," *Journal of Aircraft*, vol. 51, pp. 1604–1617, 2014.

[41] "Gradient-based optimization procedure." `https://blog.naver.com/richscskia/221940116927`.

[42] J. R. Martins and J. T. Hwang, "Review and unification of methods for computing derivatives of multidisciplinary computational models," *AIAA Journal*, vol. 51, p. 2582–2599, Nov 2013.

[43] J. Z. Kolter and T. Chen, "Algorithms and implementation automatic differentiation."

[44] B. van den Berg, T. Schrijvers, J. McKinna, and A. Vandenbroucke *Forward- or reverse-mode automatic differentiation: What's the difference?*, 2023.

[45] C. Elliott, "The simple essence of automatic differentiation," *Proceedings of the ACM on Programming Languages*, vol. 2, pp. 1–29, 2018.

[46] T. A. Albring, M. Sagebaum, and N. R. Gauger, "Efficient aerodynamic design using the discrete adjoint method in su2," *17th AIAA/ISSMO Multidisciplinary Analysis and Optimization Conference*, Jun 2016.

[47] J. Samareh, "Aerodynamic shape optimization based on free-form deformation," in *10th AIAA/ISSMO Multidisciplinary Analysis and Optimization Conference*, 2004.

[48] G. Kenway, G. Kennedy, and J. R. Martins, "A cad-free approach to high-fidelity aerostructural optimization," *13th AIAA/ISSMO Multidisciplinary Analysis Optimization Conference*, Jun 2010.

[49] S. Karpuk, Y. Liu, and A. Elham, "Multi-fidelity design optimization of a long-range blended wing body aircraft with new airframe technologies," *Aerospace*, vol. 7, p. 87, Jun 2020.

[50] F. Palacios, J. Alonso, K. Duraisamy, M. Colonno, J. Hicken, A. Aranake, A. Campos, S. Copeland, T. Economon, A. Lonkar, and et al., "Stanford university unstructured su2: An open-source integrated computational environment for multi-physics simulation and design," *51st AIAA Aerospace Sciences Meeting including the New Horizons Forum and Aerospace Exposition*, Jan 2013.

[51] P. Gomez, "Fado: Framework for aerostructural design optimization," 2020.

[52] P. Virtanen, R. Gommers, T. E. Oliphant, M. Haberland, T. Reddy, D. Cournapeau, E. Burovski, P. Peterson, W. Weckesser, J. Bright, S. J. van der Walt,

M. Brett, J. Wilson, K. J. Millman, N. Mayorov, A. R. J. Nelson, E. Jones, R. Kern, E. Larson, C. J. Carey, İ. Polat, Y. Feng, E. W. Moore, J. VanderPlas, D. Laxalde, J. Perktold, R. Cimrman, I. Henriksen, E. A. Quintero, C. R. Harris, A. M. Archibald, A. H. Ribeiro, F. Pedregosa, P. van Mulbregt, and SciPy 1.0 Contributors, "SciPy 1.0: Fundamental Algorithms for Scientific Computing in Python," *Nature Methods*, vol. 17, pp. 261–272, 2020.

[53] J. Nagawkar, J. Ren, X. Du, L. Leifsson, and S. Koziel, "Single- and multi-point aerodynamic shape optimization using multifidelity models and manifold mapping," *Journal of Aircraft*, vol. 58, p. 591–608, May 2021.

[54] "Çakir cruise missile." `https://www.roketsan.com.tr/en/products/cakir-cruise-missile`.

[55] J. D. Anderson, *Fundamentals of aerodynamics*. McGraw-Hill, 2011.

[56] B. L. Berrier, M. B. Carter, and B. G. Allan, "High reynolds number investigation of a flush-mounted, s-duct inlet with large amounts of boundary layer ingestion," tech. rep., 2005.

[57] "Bayraktar akinci." `https://baykartech.com/tr/uav/bayraktar-akinci/`.

[58] P. P. Walsh and P. Fletcher, *Gas turbine performance*. Blackwell Science, 2008.

[59] T. Hsieh, "An investigation of separated flow about a hemisphere-cylinder at incidence in the mach number range from 0.6 to 1.5," in *15th Aerospace Sciences Meeting*, 1977.

[60] E. B. Graves and R. H. Fournier, "Stability and control characteristics at mach numbers of a cruciform air-to-air missile with triangular canard controls and a trapezoidal wing." `https://ntrs.nasa.gov/citations/19740025319`, 1974. NASA Technical Reports Server (NTRS).